Cancer Nanotechnology

RESEARCH Open Access

g-C_3N_4-based photoresponsive magnetic nanocatalyst drives type-I photodynamic therapy under visible light irradiation, boosting chemo/chemodynamic synergistic therapy of colon cancer

Laya Khoshtabiat[1], Azadeh Meshkini[1,3*] and Maryam M. Matin[2,3]

*Correspondence:
a.meshkini@um.ac.ir

[1] Department of Chemistry, Faculty of Science, Ferdowsi University of Mashhad, Mashhad, Iran
[2] Department of Biology, Faculty of Science, Ferdowsi University of Mashhad, Mashhad, Iran
[3] Novel Diagnostics and Therapeutics Research Group, Institute of Biotechnology, Ferdowsi University of Mashhad, Mashhad, Iran

Abstract

Background: Fenton reaction-based chemodynamic therapy (CDT) is regarded as a highly tumor-specific treatment modality due to its intrinsic tumor microenvironment (TME)-specific targeting properties, such as high amounts of lactic acid and H_2O_2. To improve the therapeutic efficacy of CDT, in this study, a self-tracking and external stimuli-responsive Fenton nanoreactor was accompanied by type I photodynamic therapy.

Results: A cisplatin-containing H_2O_2 self-supplying heterogeneous Fenton nanocatalyst (CaO_2.CDDP@Fe_3O_4) was constructed, and it was accompanied by graphitic carbon nitride (g-C_3N_4) nanosheets as a photosensitizer. The hybrid nanocomposite was decorated with ascorbic acid, which improved the tumor-targeting capabilities of the final construct (CCFCA). Besides the generation of hydroxyl radicals ($^{\cdot}OH$) by metal-based Fenton nanocatalyst (CaO_2.CDDP@Fe_3O_4), g-C_3N_4-driven nonmetal-based Fenton reaction translated external energy into extremely lethal free radicals within the tumor cells through oxygen-independent type-I PDT. According to 2D and 3D cell culture experiments, CCFCA demonstrated cancer cell selectivity and a high cellular uptake efficiency under a static magnetic field (SMF) and visible light irradiation. Further investigations showed that CCFCA suppressed the antioxidant system and altered the mitochondrial membrane potential and consequently caspase activity, causing apoptosis in cancer cells. The enhanced tumor-inhibitory capability of the nanocomposites was shown by the increased anti-tumor activity of CCFCA in treated mice under SMF and light irradiation as compared to those treated with the free drug. Moreover, no deleterious effects on normal tissues and blood cells were observed in CCFCA-treated mice.

Conclusion: Based on the results obtained, dual Fenton reactions were provided in a simple platform (CCFCA) where the cooperative combination of multiple approaches (chemotherapy, magnetic therapy, and PDT) enhanced CDT efficiency against colon cancer.

Keywords: Chemodynamic therapy, Fenton reaction, Static magnetic field, Photodynamic therapy, g-C3N4

Background

Chemodynamic therapy (CDT) is a promising strategy for selective cancer therapy, which is mediated by the Fenton reaction, generating a unique pattern of reactive oxygen species (ROS). The low valent transition metals can initiate the Fenton reaction in tumor cells, which are rich in hydrogen peroxide (H_2O_2) and have an acidic environment. In this process, Fenton nanocatalysts convert endogenous H_2O_2 in tumor cells into highly deleterious ROS such as hydroxyl radical ($^{\cdot}OH$), resulting in tumor-selective cell death with low side effects to normal tissues (Chen et al. 2022; Rao et al. 2021; Tian et al. 2021). However, evidence showed that the effectiveness of CDT, notably in in vivo experiments, is far from satisfactory for the effective elimination of tumors (Li et al. 2021). In fact, the low level of H_2O_2 (100 μM), high potential antioxidant system, and low content of transition metals in the tumor microenvironment cause an insufficient amount of hydroxyl radicals, limiting the therapeutic benefits (Tang et al. 2021). Therefore, it is extremely desirable to develop a strategy to surmount the obstacles in CDT. Several approaches have been used so far to speed up Fenton reaction kinetic and consequently increase CDT effectiveness. To provide high enough intratumoral H_2O_2 for producing a large amount of $^{\cdot}OH$, the fabrication of a H_2O_2-filled polymersome containing a Fenton nanocatalyst has been investigated (Li et al. 2016). However, this strategy worked poorly, as evidenced by the low catalytic activity of hydrophobic Fenton nanocatalysts and leakage of H_2O_2 from wrapping materials which led to damage to normal cells. An alternative option was the in situ H_2O_2 generation within the tumor which was provided by the incorporation of glucose oxidase into the Fenton nanocatalyst (Ranji-Burachaloo et al. 2019). However, decreased oxygen concentration in hypoxic tumor microenvironments restricted the capacity of such constructions for enhancing the Fenton reaction kinetic. To tackle the challenges, H_2O_2 self-supplying CDT systems based on metal peroxide (MO_2) nanoparticles were developed (He et al. 2021). These nanoparticles including CaO_2, ZnO_2, CuO_2, MgO_2, etc. are produced as the result of replacing metal ions with hydrogen atoms of H_2O_2. MO_2 can cause a strong oxidation effect following their interaction with H_2O and generate H_2O_2 under acidic conditions. The H_2O_2 produced by MO_2 might react with Fenton metals (such as Fe^{2+}, Mn^{2+}, Cu^{+}, Co^{2+}, etc.) to form hydroxyl radical ($^{\cdot}OH$), leading to an increase in CDT efficiency (He et al. 2021; Liu et al. 2022).

$$MO_2 + 2H_2O \rightarrow H_2O_2 + M(OH)_2$$

$$Fe^{2+} + H_2O_2 \rightarrow Fe^{3+} + {}^{\cdot}OH + HO^{-}$$

$$Fe^{3+} + H_2O_2 \rightarrow Fe^{2+} + {}^{\cdot}OOH + H^{+}$$

Additionally, the released metal ions from MO_2 exhibited cytotoxic effects known as "ion-interfering therapy". The bursting of ions such as Ca^{2+} inside tumor cells damages the mitochondria, prevents the production of ATP, inhibits the biosynthesis and activity of p-glycoproteins, and reverses drug resistance in cancer (Liu et al. 2020).

Another strategy that could make the Fenton process more effective is photodynamic therapy (PDT). PDT is a therapeutic modality that produces a large amount of

site-specific ROS by a photosensitizer in the light-exposed area, resulting in cancer cell destruction (Correia et al. 2021; Dai et al. 2019; Youssef et al. 2017). Two types of PDT process, type I and II, are driven by photosensitizers (PSs) and it depends on electron or energy transfer. Several studies have focused on the design of PSs that can undergo type II photoreaction in which low excited energy is needed for singlet oxygen ($^1O_2$) generation from molecular oxygen. However, the aggravated hypoxia in the tumor microenvironment decreases the efficiency of type II-based PDT. In contrast to type II, type I PDT is oxygen-independent and produces $O_2^{\cdot-}$, $^{\cdot}OH$ or H_2O_2 via electron-transfer or hydrogen abstraction-based photoreaction. In this way, to counteract O_2-depletion, PS fully employs disproportional reaction, Haber–Weiss reaction, or Fenton reaction, to boost the effectiveness of treatment for hypoxic tumors (Chen et al. 2021a). Therefore, the development of type I photosensitizers with reduced oxygen requirement is crucial.

Among the various photosensitizers (PS), 2D graphitic carbon nitride (g-C_3N_4) is a highly promising candidate for PDT. It is a safe two-dimensional (2D) material with distinctive structural and electrical features (Davardoostmanesh et al. 2020; Zhao et al. 2021). Tri-s-triazine-based g-C_3N_4, the most stable and energetically favorable phase of g-C_3N_4, has a relatively narrow band gap (2.7 eV) and strong reduction capacity, making it a visible light photochemical catalyst. Prior studies pointed out that g-C_3N_4 as PS has the capacity to drive type-II PDT (Cui et al. 2019; Ju et al. 2016). It is based on the water-splitting capability of g-C_3N_4 that ultimately results in the generation of O_2, which not only attenuates the hypoxic status of the tumor microenvironment but also provides the possibility for singlet oxygen generation. In fact, the photo-generated holes in g-C_3N_4 can be utilized for the production of H_2O_2 and O_2; however, the two-electron process for H_2O_2 formation is preferable to the four-electron process for O_2 evolution in terms of kinetic (Liu et al. 2015). Therefore, it seems sense to classify g-C_3N_4 as a type I photosensitizer given that it can produce H_2O_2 when exposed to light. However, surface modifications are needed to improve the selectivity and activity of g-C_3N_4 toward the two-electron water oxidation and H_2O_2 production (Fattahimoghaddam et al. 2019; Wang et al. 2018).

Another challenge related to PDT is the nonspecific distribution of PSs in vivo and their inability to penetrate deeper tumors in patients' bodies which result in increased toxicity to normal cells. It has been suggested that a combination of PSs with magnetic nanoparticles like magnetite (Fe_3O_4) may tackle these limitations (Choi et al. 2017; Izadi et al. 2019; Khoshtabiat et al. 2021; Seabra 2017). When an external magnetic field is applied, magnetic nanoparticles can target specific sites (magnetic targeting) and deliver a considerable amount of therapeutic PSs to deep-state tumors. In other words, the PDT efficacy can be enhanced by the tumor being exposed to a local magnetic field.

Given the above considerations, in this study, Fenton-based therapy was accompanied by PDT, and the utilization of a magnetic field improved the collaborative therapeutic efficacy in eradicating colon cancer. A H_2O_2 self-supplying magnetic Fenton nanocatalyst containing cisplatin (CaO_2.CDDP@Fe_3O_4 named CCF) was designed and it was accompanied with g-C_3N_4 as PS (CaO_2.CDDP@Fe_3O_4.C_3N_4 named CCFC). We supposed that in situ H_2O_2 generation by CaO_2 would facilitate the Fenton reaction mediated by Fe_3O_4 nanocatalyst. Furthermore, upon LED irradiation (λ: 450 nm), excited

g-C_3N_4 can drive type-I PDT, generating a large amount of H_2O_2 and enhancing the efficiency of CCFCA against cancer cells. Herein, g-C_3N_4 nanosheets not only act as PS and maximize the yield of ROS upon irradiation but also serve as an agent for imaging and real-time monitoring of the nanosystem. In addition to applying a magnetic field to achieve "magnetic targeting", ascorbic acid (AA) was also conjugated to the drug delivery system (CaO_2.CDDP@Fe_3O_4.C_3N_4.AA, named CCFCA), providing active targeting and boosting tumor site-specific activity of the nanosystem. The physicochemical properties and biological performance of the designed nanosystem were evaluated in detail. Cellular uptake, cytotoxicity, and the mechanism of action of CCFCA were evaluated in monolayer cell culture using colorectal carcinoma cell line (CT26 cells), fibroblast cells (NIH3T3 cells), and human embryonic kidney cell line (HEK-293 cells). An ex vivo multicellular model that simulated in vivo tumor tissue was also used to analyze the nanoparticle penetration behavior into the deep-state tumors. To further illustrate the remarkable anticancer efficacy of the nanosystem, the in vivo antitumor properties were explored using CT26 tumor-bearing mice.

Materials and methods

Synthesis of CaO_2 nanoparticles containing cisplatin

CaO_2 nanoparticles were synthesized via a hydrolysis-precipitation process (Chen et al. 2021b). Calcium chloride solution (100 mg ml^{-1}, 2 ml) containing cisplatin (CDDP, 1 mg ml^{-1}) was added dropwise to polyvinylpyrrolidone solution (PVP, 10 ml, 15 mg ml^{-1}). Afterward, H_2O_2 (1.5 ml, 30%) and NH_3.H_2O (1 ml, 1 M) were sequentially added to the above mixture. After 3 h stirring, NaOH (0.5 ml, 1 M) was added to the reaction. PVP-stabilized CaO_2 nanoparticles containing CDDP were precipitated by centrifugation (7500*g*, 10 min) and rinsed with NaOH (0.1 M), deionized (DI) water, and ethanol. Finally, the nanoparticles were named CaO_2.CDDP and dried at 37 °C for 24 h.

Synthesis of CaO_2.CDDP@Fe_3O_4 nanocomposite

$FeCl_2$.$6H_2O$ solution (80 mg ml^{-1}, ethylene glycol) was added to dispersed CaO_2.CDDP nanoparticles (2 ml, ethylene glycol). Different concentrations of CaO_2.CDDP nanoparticles (12.5, 25, and 50 mg ml^{-1}) were used in this step. After 30 min stirring, CH_3COONa (450 mg ml^{-1}, ethylene glycol) was added to the reaction. The reaction continued for 30 min and then polyethylene glycol (PEG 2000) solution (0.062 g ml^{-1}, ethylene glycol) was added to the mixture and stirred for 30 min. The mixture was then transferred to a Teflon-lined stainless-steel autoclave and heated at 200 °C for 24 h. The black precipitation was separated by a magnet and rinsed with ethanol three times. The obtained nanocomposites were dried at 60 °C for 24 h. Based on the size and morphology of nanocomposites, 25 mg ml^{-1} was the optimum concentration of CaO_2.CDDP nanoparticles for the synthesis of CaO_2.CDDP@Fe_3O_4 nanocomposites (Additional file 1: Fig. SI2).

Deposition of CaO_2.CDDP@Fe_3O_4 nanocomposites on g-C_3N_4 nanosheets

The preparation of bulk and nanosheet of g-C_3N_4 has been explained in supplementary data. For deposition of CaO_2.CDDP@Fe_3O_4 nanocomposites on g-C_3N_4 nanosheets, CaO_2.CDDP@Fe_3O_4 nanocomposites (1 mg ml^{-1}) were dispersed in 5 ml H_2O:ethanol (1:1 (v:v)). Then, nanocomposites were added to 10 ml g-C_3N_4 nanosheet (2 mg ml^{-1}, DI

water) and the reaction was carried out at 40 °C under N_2 gas flow. After 4 h of stirring, the mixture was centrifuged (2700 g, 5 min), and the precipitate was rinsed with DI and ethanol, and dried at 50 °C for 24 h. CaO_2.CDDP@Fe_3O_4.C_3N_4 nanocomposites were named CCFC.

Conjugation of ascorbic acid on CaO_2.CDDP@Fe_3O_4.C_3N_4

Ascorbic acid (AA) was dissolved in 5 ml H_2O:ethanol (v:v) and it was added to 5 ml of dispersed CaO_2.CDDP@Fe_3O_4.C_3N_4 nanocomposites (H_2O:ethanol (v:v)) at 40 °C under N_2 gas flow. After 4 h of stirring, AA-conjugated nanocomposites were centrifuged and washed with DI and ethanol and dried at 50 °C for 24 h. The final construct was named CCFCA.

H_2O_2 generation assay

H_2SO_4 (0.1 M) was added to the $KMnO_4$ solution (50 μg ml^{-1}). Synthesized nanocomposites (1 mg ml^{-1}) were added to the above mixture. At different time intervals, the absorbance of the mixture was measured at 515 nm by a UV–Vis spectrophotometer. Upon H_2O_2 generation, the pink color of permanganate (MnO^{4-}) converts to the colorless Mn^{2+}. The addition of H_2O_2 to the mixture of $KMnO_4$ and H_2SO_4 was considered as a positive control.

Hydroxyl radical generation assay

3,3,5,5-Tetramethylbenzidine (TMB) solution (40 μg ml^{-1}) was prepared with different pHs (pH 7.4 (phosphate-buffered saline, PBS) and pH 5.5 (acetate buffer)). Then, the nanocomposites were added to the TMB solution without using H_2O_2. Upon $^{\cdot}OH$ generation, TMB is oxidized, giving blue-green color which was measured at 650 nm.

2D Cell culture experiments

In vitro cytotoxicity assay

Cancer or normal cells (Supporting Information) were seeded (1×10^4 cells) into 96-well tissue culture plates. After 24 h incubation, various concentrations of CCFCA, free CDDP, or bare nanocomposite (CFCA) were added to cells. Then, cell culture supernatant was thrown out after 48 h and MTT (3-(4,5-dimethylthiazol-2-yl)-2,5-diphenyltetrazolium bromide) solution (10 μl, 5 mg ml^{-1}) was added to each well. After 4 h, the MTT solution was replaced with 100 μl DMSO in each well. The absorbance of each well was measured at 570 nm using an ELISA reader (BioTek, ELX800, USA). Furthermore, to investigate the effect of static magnetic field (SMF) and LED light (λ 450 nm, 24 W) on the control cells and those treated with the nanocomposites, in all experiments, the cells were cultured in two separate 96-well tissue culture plates. After 4 h of treatment, one of the culture plates was exposed to SMF (0.9 Tesla) for 30 s, and 1 h after that, it was exposed to LED visible light radiation with a wavelength of 450 nm for 15 min (Additional file 1: Fig. SI1). The rest of the conditions were the same for the cells of both culture plates. The concentration of synthesized nanocomposites or free drugs was calculated for 50% cell viability (IC_{50}) and its validation was done with GraphPad Prism 6 software.

Live & dead assay

Acridine orange & ethidium bromide staining

CT26 cells (1×10^4 cells) were exposed to CCFCA or free CDDP for 48 h. For the detection of live and dead cells, acridine orange (AO, 4 μg ml^{-1}) and ethidium bromide (EtBr, 4 μg ml^{-1}) were added to cells, respectively, and the images were captured by a fluorescent microscope (Olympus, Japan).

Sub-G1 assay

Propidium iodide (PI, 20 μg ml^{-1}) solution containing Triton X-100 (0.5 μl ml^{-1}), sodium citrate (10 mg ml^{-1}), and RNase (20 μg ml^{-1}) was added to treated and untreated cells. After 30 min at 37 °C, stained cells were analyzed by flow cytometry (BD Biosciences, USA), and the percentage of cells at the sub-G1 phase was determined using FlowJo v10 software.

Cellular uptake studies

Evaluation of cellular uptake by inductively coupled plasma optical emission spectrometer (ICP-OES)

Intracellular CDDP was measured by ICP-OES. For this purpose, cells were treated with free CDDP or CCFCA for 8 h. Then, cell lysate was prepared after mixing treated cells with cold lysis buffer (130 μl, Triton X-100 (1%), Tris–HCl (50 mM), and NaCl (150 mM)). After 30 min of incubation, the mixture was centrifuged and the supernatant was considered for assessment of intracellular Pt. Finally, the amount of Pt was normalized to total protein content which was determined by the Bradford method (Kruger 1994).

Perl's Prussian blue staining

Intracellular deposited iron was detected by Perl's Prussian blue staining. CT26 cells were treated with CCFCA for 24 h. Then, ferrocyanide solution (potassium ferrocyanide trihydrate (20%) and hydrochloric acid (20%)) was added to cells and incubated for 20 min. After the formation of Prussian blue pigment (insoluble blue compound), cells were washed with DI water. To stain cytoplasm, a neutral red solution (neutral red dye (0.03 M), sodium acetate (0.03 M), and acetic acid (0.02 M)) was added to the cells. After 5 min of incubation, stained cells were washed and the images were taken by an inverted light microscope (TCM 400-LABOMED, USA).

Evaluation of intracellular reactive oxygen species (ROS)

For the detection of intracellular ROS, 2',7'-dichlorodihydrofluorescein diacetate (DCFH-DA) solution (10 μmol/l) was added to the cells. After 30 min of incubation at 37 °C, the cells were rinsed with PBS, and the green fluorescence emission of oxidized DCFH was evaluated by a flow cytometer.

Mitochondrial membrane potential assay

For assessment of the mitochondrial membrane potential, cationic fluorescent dye, rhodamine-123 (Rh-123, 5 μg ml^{-1}), was added to cells. After 1 h of incubation at 37 °C, cells were washed with PBS, and the green fluorescence emission of Rh-123 was analyzed by

a flow cytometer. Loss of mitochondrial membrane potential results in a reduction in fluorescence intensity.

Caspase-3 activity assay

Analysis of caspase-3 activation in treated and untreated cancer cells was performed by indirect immunofluorescence staining. After treatment of cells with CCFCA for 48 h, trypsinized CT26 cells were washed with PBS, permeabilized, and blocked with a blocking buffer containing 1X PBS, 0.01% Triton X-100, and 1% BSA for 10 min prior to incubation with a primary antibody (cleaved caspase-3 antibody) for 1 h. After unconjugated antibody removal by rinsing with PBS, the cells were exposed to a secondary immunoglobulin G fluorescein isothiocyanate-conjugated antibody for 30 min. Followed by 3 washes with PBS, the fluorescence intensity of the stained cells was analyzed by FACS (Meshkini and Oveisi 2017).

3D cell culture experiment

Multicellular tumor spheroid model

CT26 spheroids were produced by the liquid overlay method as previously described (Pereira et al. 2017). Briefly, autoclaved agarose solution (1.5%) was poured into 96-well plates to generate a gel pad at the bottom of the wells. Then, CT26 cells (1×10^3 cells/well, 100 µl) were added into agarose-coated wells. The plate was shaken slowly for 10 min and put back in the incubator (5% CO_2, humidified atmosphere, and 37 °C) for 2 days. Afterward, the cell culture supernatant was replaced with a fresh medium containing drug-loaded nanocomposites or free drug. Spheroid volume was calculated according to Eq. (1),

$$\text{Spheroid volume} = \frac{4}{3}\pi r^3 \tag{1}$$

$$r = \frac{1}{2}\sqrt{d_1 d_2}$$

where d_1 and d_2 are the diameters of a spheroid.

Evaluation of cell viability in spheroids

Spheroids were treated with CCFCA for 7 days. Then, the spheroid structure was disintegrated by pipetting and mixing them with trypan blue. The number of viable and non-viable cells was determined using a hemocytometer.

In vivo anti-tumor experiments

Experimental design

Healthy female BALB/c normal mice (6–8 weeks old) were used for all animal experiments according to a protocol approved by the Institutional Animal Care and Use Committee at Ferdowsi University of Mashhad (Document no: IR.UM.REC.1399.128).

Generation of CT26 tumor model

For the construction of the CT26 tumor model, subcutaneous injection of CT26 cell suspension (100 µl PBS containing 2×10^6 cells for each mouse) was carried out into the right flank of the mice. As the tumor volume in mice reached approximately 110 ± 5 mm^3, the animals were treated with free CDDP or fabricated samples. In this line, tumor-bearing mice were randomly divided into seven groups (n = 5) and given an intravenous injection of either free CDDP, CFCA, or CCFCA based on Additional file 1: Table SI3. All mice received three times of intravenous injections on days 1, 4, and 7 with corresponding agents (PBS (pH 7.4) for the control group). For the experiments under SMF and LED irradiation, 30 min after PBS or CCFCA administration, the mice were subjected locally at the tumor site to SMF for 10 min. After 30 min of rest, they were exposed to blue LED light for 15 min.

The tumor volume was calculated using the following formula:

$$\text{Tumor volume} = 0.5 \times \text{lenght} \times (\text{width})^2$$

The weight of mice and tumor volumes were recorded every two days. At 14 days post-treatment, the animals were sacrificed to collect the tumors and main organs (heart, liver, lung, spleen, and kidney). After being weighed and photographed, the tumor tissues were fixed in formalin solution (10%) for further examination with hematoxylin and eosin (H&E) staining.

In vivo fluorescence imaging and biodistribution assay

CT26 tumor-bearing mice were intravenously injected with CCFCA nanocomposite. After 24 and 48 h post-injection, the animals were sacrificed and a plane of tissues was harvested. Fluorescence images were captured using a small animal in vivo imaging system (IVIS, PerkinElmer Inc, Watham, USA) ($\lambda_{excision}$: 470 nm, $\lambda_{emission}$: 600 nm).

Hematology assay

CT26 tumor-bearing mice were intravenously injected three times with CCFCA nanocomposite or PBS (control). At 14 days post-treatment, blood was collected from mice and placed into anticoagulant tubes for routine blood tests. Blood biochemistry analyses were performed at Dr. Norouz Pour medical laboratory.

Results and discussion

Synthesis and characterization of CCFCA nanocomposite

The CCFCA preparation procedure is depicted in Scheme 1, wherein the CaO_2-containing CDDP nanoparticles were firstly fabricated as a H_2O_2-self-supplying CDT platform. Based on ICP-OES analysis, the content of CDDP in nanoparticles was calculated to be 2.027 ± 0.132 µg per mg of nanoparticles (Additional file 1: Table SI1). Moreover, PVP was also used during the synthesis of CaO_2 as a surface modifier to stabilize CaO_2 nanoparticles, preventing the hydrolysis of CaO_2 in water. Then, a magnetic layer (Fe_3O_4) was formed on the surface of CaO_2.CDDP nanoparticles by ferric chloride and PEG using the decomposition method to obtain CaO_2.CDDP@Fe_3O_4 (CCF) nanocomposites with magnetic properties. Subsequently, CCF nanocomposites were deposited onto g-C_3N_4 nanosheets to obtain CaO_2.CDDP@Fe_3O_4.C_3N_4 (CCFC) with

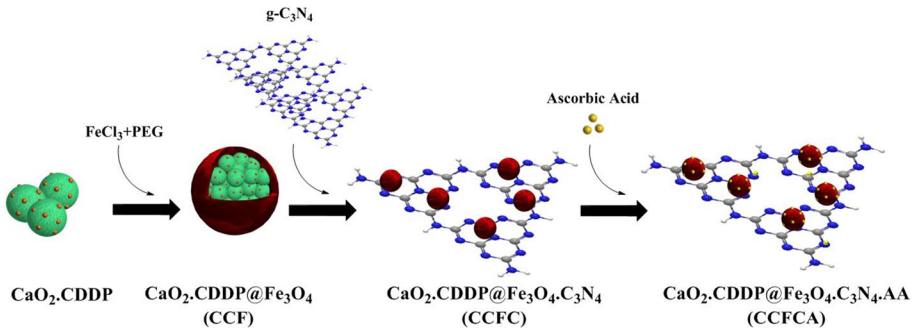

Scheme 1 Schematic illustration of different steps in CCFCA preparation

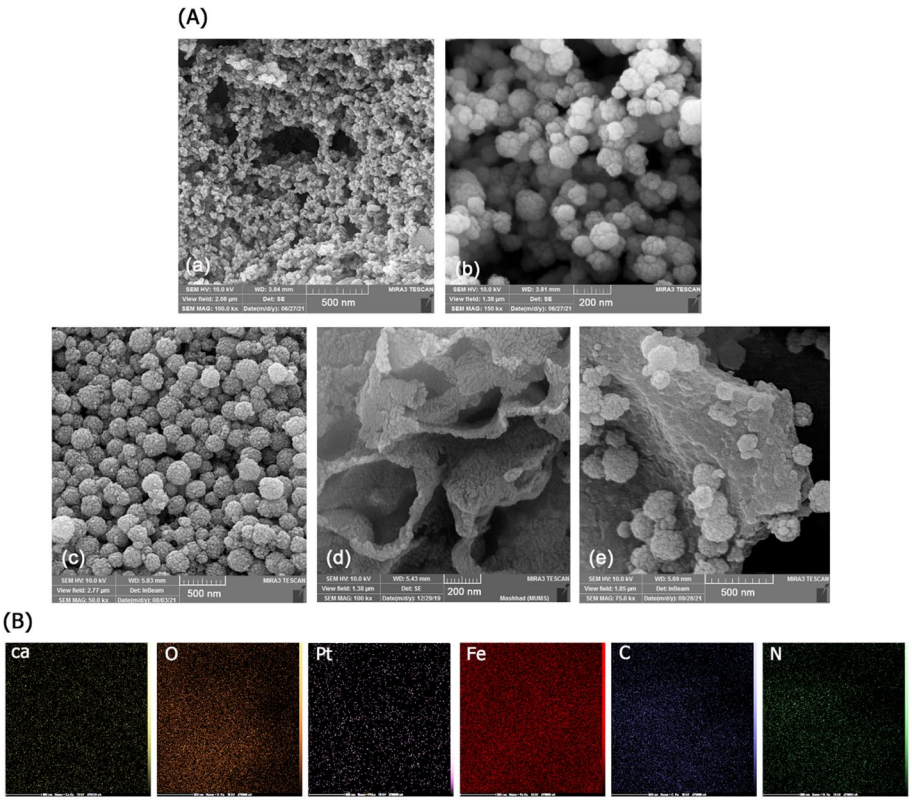

Fig. 1 FE-SEM images of fabricated nanocomposites. **A** FE-SEM image of CaO_2.CDDP (**a**), Fe_3O_4 (**b**), CaO_2.CDDP@Fe_3O_4 (**c**), g-C_3N_4 nanosheets (**d**), CaO_2.CDDP@Fe_3O_4.C_3N_4.AA (**e**). **B** Elemental mapping of CaO_2.CDDP@Fe_3O_4.C_3N_4.AA

photocatalytic activity. Finally, the outer surface of CCFC nanocomposites was functionalized with ascorbic acid (AA) to get CaO_2.CDDP@Fe_3O_4.C_3N_4.AA (CCFCA) nanocomposite with the tumor-targeting property.

To examine the structure and morphology of the synthesized nanocomposite at each stage of synthesis, FE-SEM images of the samples were prepared and the diameter of the nanoparticles was measured with ImageJ software (Additional file 1: Fig. SI2). Based on the images obtained, the CaO_2.CDDP nanocomposite (Fig. 1A(a)) showed a uniform spherical structure with a diameter of 28.55 ± 3.61 nm. To synthesize CaO_2.CDDP@

Fe_3O_4 (CCF) nanocomposite, different concentrations of CaO_2.CDDP nanoparticles were used. FE-SEM images revealed that with increasing the concentration of CaO_2.CDDP nanoparticles up to 50 mg ml^{-1}, the size of the nanocomposite became smaller and the structure of the nanocomposite became more regular (Fig. 1A(b) and Additional file 1: Fig. SI2). The optimum concentration of CaO_2.CDDP was 25 mg ml^{-1}, resulting in the formation of a more regular, uniform, and smaller spherical core–shell structure (diameter 173.58 ± 19.01 nm, Additional file 1: Fig. SI2(C)) compared to Fe_3O_4 nanoparticles (diameter 217.97 ± 34.40 nm). At 50 mg ml^{-1} of CaO_2.CDDP nanoparticles, the structure of nanocomposites was destroyed. Therefore, the nanocomposite consisting 25 mg ml^{-1} of CaO_2.CDDP was used to continue the process of synthesis.

CaO_2.CDDP@Fe_3O_4 nanocomposites were then deposited on the surface of exfoliated g-C_3N_4. Bulk g-C_3N_4 was synthesized from the thermal polymerization of melamine and it was exfoliated into thin layers through the hydrothermal oxidation exfoliation in the sodium hypochlorite solution which is a safe and environmental-friendly method (Fig. 1(d)). Note that the exfoliation of g-C_3N_4 provides a large specific surface area and improves the photocatalytic performance of nanosheets as compared to the parent bulk form (Cui et al. 2018). Figure 1A(e) and SI3 disclosed the successful deposition of CaO_2.CDDP@Fe_3O_4 nanocomposites on g-C_3N_4 nanosheets. Finally, nanocomposites were functionalized with AA for delivery of the nanosystem to cancer cells. A growing number of studies have demonstrated that AA can selectively kill cancer cells while normal cells remain resistant (An et al. 2013; Chen et al. 2008). AA can target glucose transporters (Gluts) which are overexpressed on the surface of certain cancers (Ngo et al. 2019). In fact, released ROS from cancer cells facilitate the oxidation of ascorbic acid to dehydroascorbic acid (DHA) in the extracellular space of tumor cells and it can be taken up by the cells through Gluts. Note that Glut1 and Glut3 have a higher affinity for DHA than glucose (Ngo et al. 2019).

Elemental mapping of CaO_2.CDDP@Fe_3O_4.C_3N_4.AA also confirmed the presence of Ca and Pt elements in the structure of CaO_2.CDDP nanoparticles, Fe element was related to the magnetic layer of the nanocomposite, and C and N elements were related to g-C_3N_4. C element was also attributed to AA (Fig. 1B).

The FT-IR spectrum of fabricated samples was also investigated. In the absorption spectrum of CaO_2 (Fig. 2A (a)), the bands at 578 and 872 cm^{-1} corresponded to stretching vibrations of O-Ca-O and O–O, respectively. The broad band between the wavenumbers 1300 and 1700 cm^{-1} was related to the bending vibration of O-Ca-O (Khorshidi et al. 2020). The bands at 3444 and 1667 cm^{-1} were attributed to stretching and bending vibrations of N–H of CDDP, respectively, signifying the presence of CDDP in the structure of CaO_2.CDDP nanocomposite (Fig. 2A(b)). In the absorption spectrum (c), two characteristic bands emerged at 576 and 3403 cm^{-1} assigned to the stretching vibrations of Fe–O and O–H, respectively, which were related to Fe_3O_4 in the structure of nanocomposite. In the absorption spectrum (d), the typical IR band of g-C_3N_4 was observed at 809 cm^{-1} corresponding to the vibrations of the tri-s-triazine ring system. The bands with wavenumbers ranging from 1249 to 1700 cm^{-1} (1249, 1324, 1413, 1573, and 1639 cm^{-1}) were characteristic stretching vibration modes of C=N and C-N heterocycles of g-C_3N_4 (Cui et al. 2018), indicating the successful conjugation of CaO_2.CDDP@Fe_3O_4 nanocomposites on g-C_3N_4 nanosheets. The distinctive absorption peak

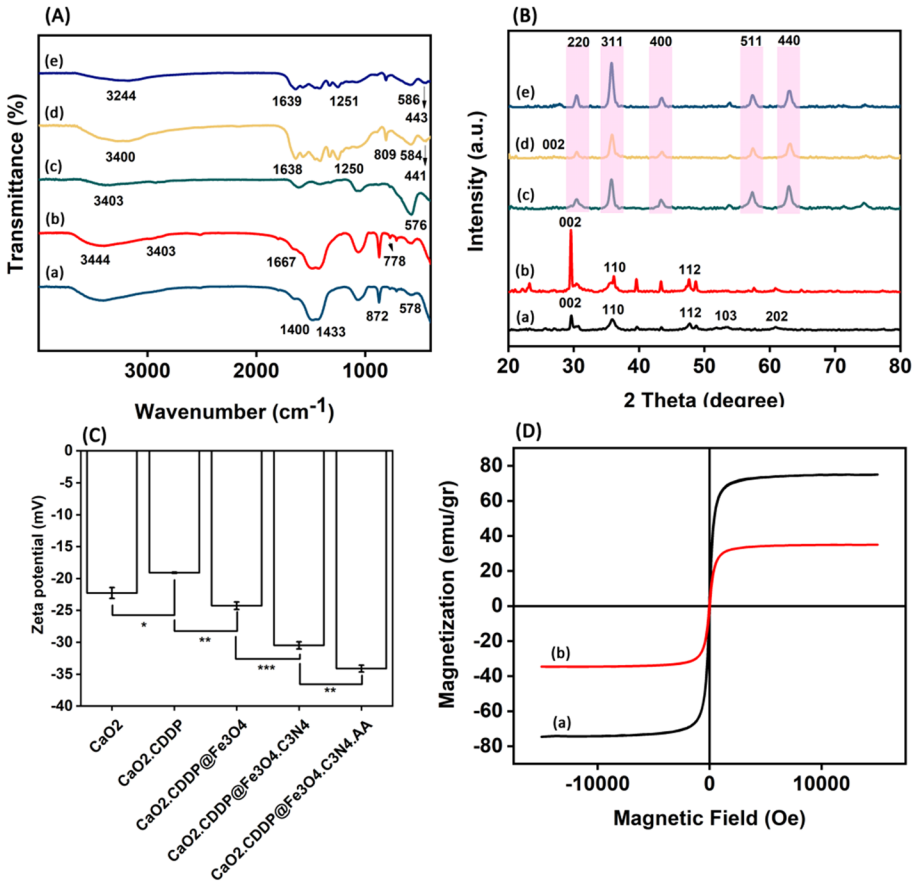

Fig. 2 Characterization of CCFCA nanocomposite. **A** FT-IR and (B) XRD spectra of fabricated samples. **a** CaO_2 nanoparticles, **b** CaO_2 containing CDDP (CC), **c** CaO_2.CDDP@Fe_3O_4 (CCF), **d** CaO_2.CDDP@Fe_3O_4.C_3N_4 (CCFC), **e** CaO_2.CDDP@Fe_3O_4.C_3N_4.AA (CCFCA). **C** Zeta potential analysis of fabricated samples at pH 7.4. **D** VSM magnetization curve of nanocomposites, (**a**) CCF and (**b**) CCFCA

at 1752 cm^{-1} in ascorbic acid spectra (Additional file 1: Fig. SI4) was caused by stretching vibrations of the C = O of the five-membered lactone ring, and this band disappeared in the spectrum of the nanocomposites containing ascorbic acid (Fig. 2A(e)). Moreover, the C = C stretching band shifted from 1667 to 1639 cm^{-1} in the nanocomposite, indicating successful conjugation of ascorbic acid to the surface of the nanocomposite.

The crystalline nature of fabricated nanocomposites was investigated by X-ray crystallography. In the XRD pattern of CaO_2 nanoparticles (Fig. 2B(a)) five Bragg reflections at 29.7˚, 35.9˚, 47.7˚, 52.9˚, and 60.9˚ were observed, corresponding to the planes (002), (110), (112), (103) and (202), respectively, which were matched with the reference pattern of crystalline CaO_2 (JCPDS cards no.03–0865). The peaks related to planes in the structure of CaO_2.CDDP nanocomposite became sharper as cisplatin was used during the synthesis of CaO_2 nanocomposite, demonstrating a more crystallized structure (Fig. 2B(b)). The characteristic diffraction peaks of Fe_3O_4 were observed at 30.4˚, 35.7˚, 43.3˚, 53.1˚, 57.3˚, and 62.9˚ which were assigned to the planes (220), (311), (400), (422), (511), and (440), respectively, and perfectly matched with the spinel ferrite phase of Fe_3O_4 (JCPDS cards no. 019–0629) (Fig. 2B(c)) (Song et al. 2019). It implied that there were no undesirable and unwanted phases such as the hematite phase and iron

hydroxides during the synthesis of the magnetic layer of the nanocomposite. The only indicative peak in the XRD spectrum of g-C_3N_4 (002) was observed at 26.9° (JCPDS cards no. 1526–87) (Fig. 2B(d)) (Cui et al. 2018). Unlike the bulk sample, this peak was very weak in the nanosheet samples, which indicated a better layering of the sample. Moreover, the binding of ascorbic acid molecules to the synthesized nanocomposite did not impact the crystalline nature of the nanocomposite, and the index peaks related to CaO_2.CDDP@Fe_3O_4.C_3N_4 nanocomposite were evident (Fig. 2B(e)).

Zeta potential analyses revealed that CaO_2 nanoparticles possessed a surface with negative charge (-21.94 ± 0.96 mV) (Fig. 2C) (Gao et al. 2019; Huang et al. 2021); however, it changed to less negative charge values as CDDP was employed in their structure (−19.07 ± 0.08 mV). It may be related to the amine group of CDDP. The surface charge of CaO_2.CDDP nanoparticles shifted back to more negative values (−24.27 ± 0.58 mV) as a magnetic layer was added. Deposition of CaO_2.CDDP@Fe_3O_4 nanocomposites onto g-C_3N_4 nanosheets resulted in a high negative charge value (-30.46 ± 0.55 mV). The high stability and dispersion of planar g-C_3N_4 nanoparticles are due to the negative charge on the surface of these nanoparticles. More negative charge value (-34.12 ± 0.53 mV) was observed following the addition of AA to the nanocomposites which was due to the presence of ionizable hydroxyl group (pKa 4.2) of AA, causing a negative charge at pH 7.4 (Sreeja et al. 2015).

To study the magnetic behavior of the nanocomposites, VSM analysis was performed (Fig. 2D). The results showed that by increasing the field intensity up to 15,000 Oe, the magnetic properties of CaO_2.CDDP@Fe_3O_4 nanocomposite enhanced up to 75.04 emu/g while this value decreased to 34.98 emu/g as g-C_3N_4 and AA were added. The non-formation of the residual loop showed that the nanocomposite had magnetic orientation in the presence of the field, which was disturbed when the field was removed. So, it could be concluded that the synthesized nanocomposite is a superparamagnetic particle.

The photocatalytic performance of CCFCA and production of H2O2 and ·OH radicals

It is a relatively safe and efficient way to generate H_2O_2 near the CDT Fenton catalysts as the concentration of H_2O_2 within tumor cells is not high enough for producing a large amount of ·OH radicals to kill cancer cells. The CCF (CaO_2.CDDP@Fe_3O_4) moiety of CCFCA nanocomposite is a Fenton-type metal peroxide that has the ability to generate H_2O_2 as demonstrated by the potassium permanganate-based colorimetric method. The amount of 0.782 μM H_2O_2 was produced by CCFCA after 2 h reaction time which was due to the presence of peroxo group of CaO_2; however, this value increased up to 1.707 μM under light irradiation (Fig. 3A and Additional file 1: Fig. SI5). The later finding indicated the generation of H_2O_2 in the photocatalytic process. The generation of ·OH radicals through the Fenton reaction in CCFCA nanocomposite was evaluated by TMB assay upon light irradiation. CCFCA showed the highest production rate of ·OH in mildly acidic conditions, but not in neutral conditions (Fig. 3B and Additional file 1: Fig. SI5). In fact, acidic pH favored metal peroxide dissociation and H_2O_2 production. These phenomena consequently speeded up Fenton reaction and ·OH generation, suggesting CCFCA as an appropriate nanocomposite for cancer treatment through H_2O_2 self-supplying CDT. Since H_2O_2 and ·OH generation enhanced upon light irradiation, we were intrigued to monitor the ability of g-C_3N_4 to generate H_2O_2 in a time-dependent manner

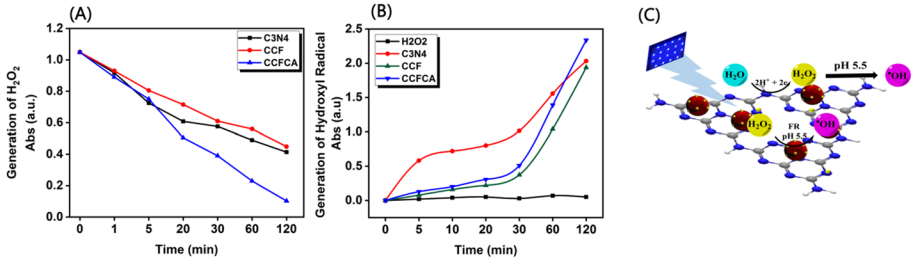

Fig. 3 Generation of H_2O_2 and hydroxyl radicals by CCFCA nanocomposites in the presence of light irradiation. **A** Kinetic rate profile of H_2O_2 generation by g-C_3N_4 nanosheets, CaO_2.CDDP@Fe_3O_4 (CCF), and CCFCA nanocomposites after light irradiation measured by a potassium permanganate-based colorimetric method. **B** Kinetic rate profile of ˙OH generation by H_2O_2 and fabricated samples. **C** Schematic illustration of ˙OH generation by CCFCA nanocomposite under light irradiation. H_2O_2 self-supplying CaO_2.CDDP@Fe_3O_4 nanocomposites execute the Fenton reaction and g-C_3N_4 nanosheets drive type I PDT and generate H_2O_2 and ˙OH, executing a Fenton-like reaction upon light irradiation

in the presence and absence of light irradiation (Additional file 1: Fig. SI6(A)). After 2 h reaction time, 0.121 μm H_2O_2 was detected by g-C_3N_4 in the absence of irradiation and a significant improvement in the production rate, of approximately 1.042 μm H_2O_2 was observed as g-C_3N_4 excited by light irradiation. In fact, H_2O_2 molecules were formed from the adsorptive H_2O on g-C_3N_4 by a two electron transfer route under irradiation. Moreover, according to the photocatalysis performance of g-C_3N_4, a large number of ˙OH radicals was detected following the decomposition of H_2O_2, realizing type-I PDT (Additional file 1: Fig. SI6(B)).

$$C_3N_4 + h\nu \rightarrow e^- + h^+$$

$$2H_2O + 2e^- \rightarrow H_2 + 2OH^-$$

$$2H_2O + 2h^+ \rightarrow H_2O_2 + 2H^+$$

$$H_2O_2 \rightarrow 2\,^{\cdot}OH$$

2D-in vitro *cytotoxicity studies*

To investigate the cytotoxicity of the synthesized nanocomposites and their effectiveness compared to the free drug (CDDP), CT26 (mouse colon cancer cells), NIH3T3 (normal mouse embryo fibroblast cells), and HEK-293 (normal human fetal kidney epithelial cells) were used. In terms of cell viability (%), the results are displayed in Fig. 4 as a function of free drug or CCFCA concentration. Free CDDP lowered the cell survival of treated cells in a dose-dependent manner (Fig. 4A); however, when it was administered by the proposed nanocarrier, the cytotoxicity against CT26 cells was dramatically amplified (Fig. 4B). The half maximum inhibitory concentration (IC_{50}) was found to be 2.84 ± 0.08 μg ml^{-1} and 0.437 ± 0.01 μg ml^{-1} for free CDDP and CCFCA nanocomposite, respectively (Additional file 1: Table SI2). Note that free CDDP did not show statistically significant cytotoxic effects on CT26 cells

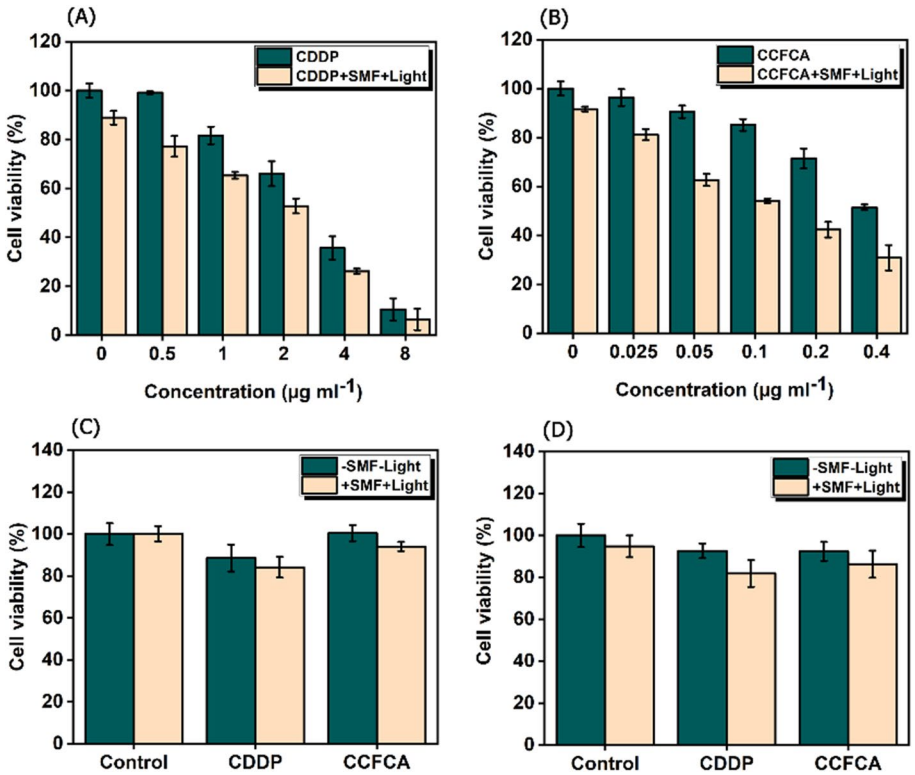

Fig. 4 Cytotoxic effects of free CDDP and CCFCA nanocomposite on colorectal carcinoma and normal cells. Cellular viability of CT26 cells treated with **A** free CDDP and **B** CDDP-loaded nanocomposite (CCFCA). Cellular viability of **C** HEK-293 cells and (D) NIH3T3 cells treated with the free drug and CCFCA nanocomposites with IC_{50} concentrations obtained from experiments related to cancer cells

at 0.437 μg ml^{-1}, and at similar condition, a minor reduction in cell survival was observed in bare nanocarrier-treated cells (Fig. 4A and Additional file 1: Fig. SI7). Moreover, the cytotoxicity of CCFCA was evaluated after exposure to SMF and LED light irradiation since it possessed both magnetic and photocatalytic activities. Following exposure to SMF and light irradiation, cell viability declined substantially as the concentration of CCFCA nanocomposites increased. The IC_{50} values were calculated as 2.15 ± 0.07 μg ml^{-1} and 0.123 ± 0.005 μg ml^{-1} for free CDDP and CCFCA nanocomposite, respectively. It should be mentioned that exposure of tumor cells to SMF (0.9 T) for 15 s was found to be toxic (94 ± 1.2% cell viability) as compared to untreated cells (99 ± 1.3% cell viability) (Additional file 1: Fig. SI8). It has previously been shown that SMF can affect cell signaling and metabolism remotely, increasing the effectiveness of drugs against cancer cells at low doses (Alavi and Meshkini 2018; Chen et al. 2010; Hajipour Verdom et al. 2018). Besides, SMF exhibits higher damaging effects when cells are treated with a nanosystem with magnetic properties. Magnetic nanoparticles have a tremendous capacity to absorb magnetic field energy, allowing them to move and vibrate inside cells, causing irreversible cell damage (Li et al. 2017; Lopez et al. 2022).

Irradiation of CT26 with LED light (w/cm^2) for 15 min did not show statistically significant cytotoxic effects (95.5 ± 2.8% cell viability, $p > 0.05$, Additional file 1: Fig. SI8);

however, exposure of CCFCA-treated cells to LED light caused tumor cell cytotoxicity enhancement which is due to the photocatalytic activity of nanosystem (Additional file 1: Fig. SI9). Based on these results it seems that besides the cytotoxic effects of CDDP, the magnetic property and photocatalytic activity of the CCFCA nanosystem significantly impact on cell survival reduction rate.

The cell viability of normal mouse fibroblast cells and human fetal kidney cells treated with CDDP and CCFCA nanocomposites was examined in the presence and absence of SMF and LED light irradiation. The graphs in Fig. 4C and D revealed no significant difference in the viability of cells treated with CCFCA even in the presence of SMF and light irradiation as compared to that of untreated cells. While free CDDP induced significant cytotoxic effects on HEK-293 cells (15.8%) and NIH3T3 (18.15%) in the presence of SMF and light irradiation. Since CCFCA nanocomposites exhibited a pH-responsive drug release behavior (Additional file 1: Fig. SI10), their selective toxicity to tumor cells was logical.

Cellular uptake of CCFCA

Fabrication of nanosystems with fluorescence emission property is a useful strategy for tracking nanosystem's cellular internalization and improving the desired targeting accuracy (Zingale et al. 2022). In this line, the PL spectrum of exfoliated g-C_3N_4 nanosheets demonstrated a blue shift performance in comparison to the bulk sample, which was attributed to the reduction in conjugation length and the strong quantum confinement effect (Additional file 1: Fig. SI11(A)). The blue fluorescence emission of g-C_3N_4 was also indicated by a fluorescence microscope (Additional file 1: Fig. SI11(B)). Since CCFCA possessed an intrinsic fluorescence emission, its internalization into the cells was examined under the fluorescence microscope (Fig. 5A). Fluorescence images showed that CCFCA-treated cells successfully internalized the nanosystem; however, in the presence of SMF and light irradiation, a higher density of nanocomposites entered the cells and distributed mainly in the cytoplasm and even broke through the nucleus envelope to enter the nucleus. The penetration of the magnetic part of CCFCA into the cells was also qualitatively visualized by Perl's Prussian blue staining (Fig. 5B). Cells were seen in red and magnetic nanoparticles in dark blue. Similarly, the results demonstrated that the introduction of SMF and light irradiation to CCFCA-treated cells led to a higher uptake of nanocomposites into cancer cells, showing more blue deposition. It has previously been reported that SMF alone has an influence on the ultrastructure of the cell surface, causing small circular holes with a diameter of 200 nm, and facilitating cellular internalization of chemotherapy drugs (Chen et al. 2010). Furthermore, it has been proved that magnetic field caused greater penetration of magnetic nanoparticles into the cells besides its effects on the expression of some proteins like clathrin which is involved in cellular uptake of nanoparticles (Chaudhary et al. 2013). The contribution of light irradiation on cellular uptake efficiency has previously been demonstrated as it impacts on cell membrane permeability; however, it depends on the wavelength of irradiated light and exposure time (Yao et al. 2017).

Cellular trafficking of CDDP was analyzed by ICP-OES, measuring intracellular Pt concentration (Fig. 5C). As it is evident, cellular uptake of CDDP was enhanced as it was delivered by the nanosystem (0.104 ± 0.002 ppm/mg protein) as compared with

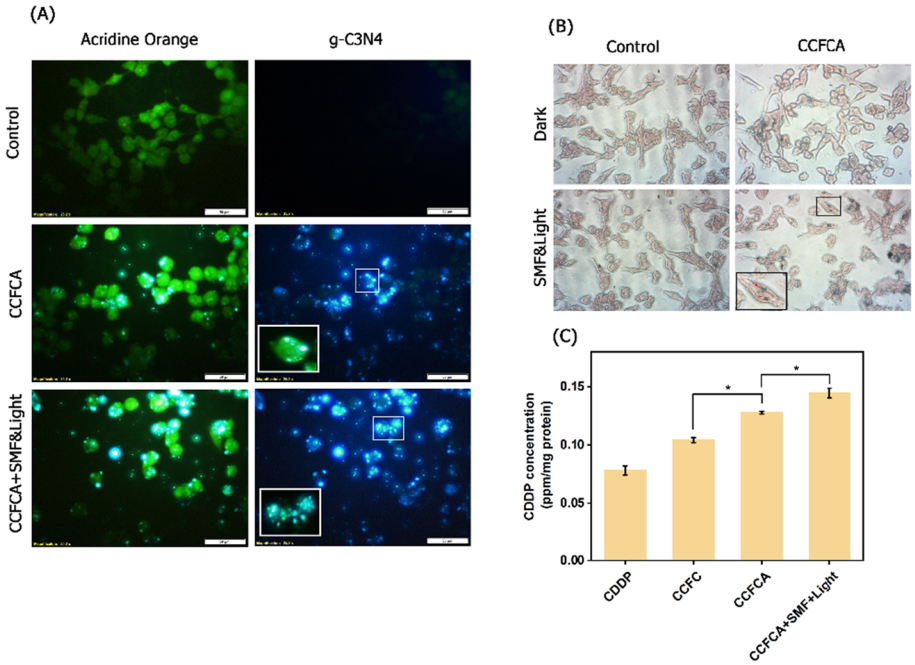

Fig. 5 Cellular internalization of CCFCA nanocomposites and free CDDP in the presence and absence of external stimuli, SMF & light irradiation. **A** Images of cells treated with CCFCA for 8 h captured by a fluorescent microscope. The viable cells were detected by acridine orange staining, emitting green fluorescence. Cellular trafficking of CCFCA nanocomposite was monitored by innate blue fluorescence emission of g-C_3N_4 nanosheets in the nanocomposites. The scale bar in all images is 50 µm. **B** Cellular internalization of the magnetic part of the CCFCA nanocomposite was evaluated by Perl's Prussian blue staining. Blue dots within the cells are related to ferric ions. **C** Cellular uptake of free CDDP and CDDP-containing nanocomposites was evaluated by ICP-OES (** $p < 0.001$, * $p < 0.01$)

free CDDP (0.078 ± 0.003 ppm/mg protein). The cellular uptake efficiency of CDDP increased after the introduction of the targeted ligand AA (0.127 ± 0.001 ppm/mg protein). This result could be attributed to the specific interaction between AA and overexpressed Gluts on the surface of CT26 cells, providing tumor-specific targeting. Correspondingly, Guney et al. conjugated AA to solid lipid nanoparticles, leading to the efficient delivery of nanosystems to cancer cells (Güney et al. 2014). Exposure of CCFCA-treated cells to SMF and light irradiation promoted cellular uptake efficiency up to 0.144 ± 0.004 ppm/mg protein, indicating the significant role of external stimuli in cellular internalization of the nanosystems.

Induction of apoptosis following disruption of intracellular redox balance

Mitochondria are essential subcellular organelles that govern cellular energy and metabolism and play an important role in cell death. As tumor cells suppress apoptotic pathways, developing a nanosystem that facilitates drug transport to mitochondria for driving apoptosis signaling pathways might be a promising cancer therapy strategy (Tabish and Hamblin 2021; Xu et al. 2022). In this line, mitochondrial targeting was monitored by assessment of the membrane polarization status of mitochondria, staining treated cells with Rh-123. It is a green fluorescence dye that is readily sequestrated in active mitochondria and emits green fluorescence, while it diffuses out of mitochondria

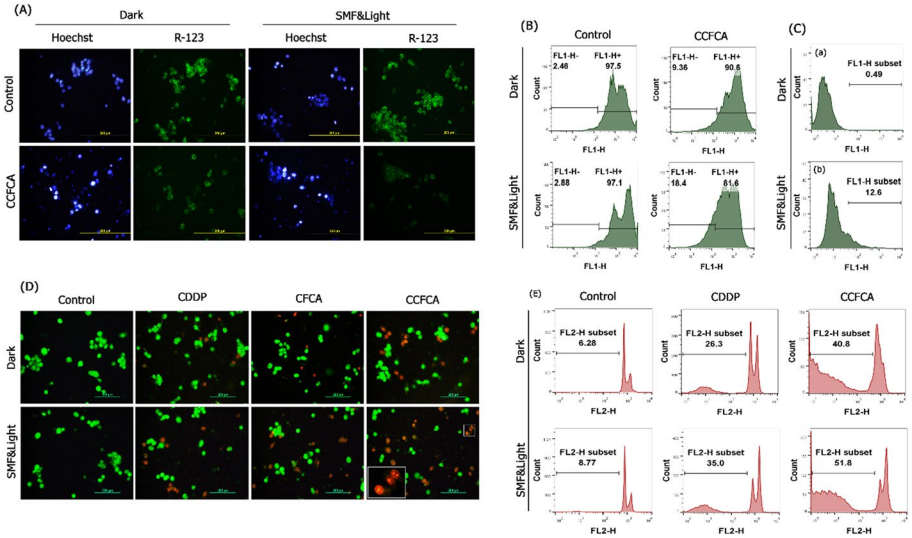

Fig. 6 Detection of the intrinsic apoptosis pathway in CCFCA-treated cells. **A** Fluorescence images of mitochondrial membrane depolarization after 4 h exposure of cells to CCFCA, using Rh-123 probe (magnification 400 x, Scale bar 200 µm). **B** Quantitative analysis of green fluorescence intensity by flow cytometry. **C** Analysis of caspase 3 activation in untreated (**a**) and CCFCA-treated cells (**b**) after 48 h incubation in the presence of SMF & light by indirect immunofluorescence assay, using anti-cleaved caspase 3 antibody. **D** Detection of apoptosis after 48 h incubation of cells with free drug, bare nanocomposite, and drug-containing nanocomposite, using AO/EtBr (magnification 200×, Scale bar 200 µm). **E** Evaluating the percentage of cells at SubG1 phase of cell cycle after 48 h incubation with free CDDP and CCFCA

upon depolarization. As shown in Fig. 6A and B the intensity of green emissions decreased as cells were treated with CCFCA, indicating mitochondrial depolarization. However, a significant shift was observed to a lower Rh-123 fluorescence area in the histogram as CCFCA-treated cells were exposed to SMF and light irradiation. It has previously been shown that g-C_3N_4 accumulated in mitochondria and led to both structural and functional loss of mitochondria under irradiation (Yadav et al. 2022; Zhang et al. 2020). Furthermore, the static magnetic field can decrease mitochondrial membrane potential, cause oxidative stress, and drive apoptotic signaling pathways [35,36]. Similar effects can also translate to cells as magnetic nanoparticles can be manipulated remotely by an external magnetic field (Murros et al. 2019).

Since there is a correlation between mitochondrial membrane depolarization and caspase activation, the amount of active caspase 3 was evaluated by indirect immunofluorescence assay, using anti-cleaved caspase 3. Histograms shown in Fig. 6C disclosed a significant increase in the amount of active caspase 3-positive cells (12.6%) in treated cells with CCFCA plus SMF and light irradiation as compared to those treated with just external stimuli. Since the activation of caspase 3 is a key event in the apoptotic process, the extent of apoptosis was evaluated and detected in CCFCA-treated cells (Fig. 6D). Fluorescence images of AO/EtBr stained cells revealed a high percentage of late apoptotic cells (orange fluorescence emission with condensed or fragmented chromatin in nuclei) in the cells treated with CCFCA as compared to those treated with bare nanocomposites or free CDDP. The percentage of orange fluorescence emitted cells increased as CCFCA-treated cells were affected by SMF and light irradiation. To quantify the incidence of apoptosis, the percentage of cells in SubG1 phase was analyzed using flow

cytometry. The results in Fig. 6E demonstrated that the percentage of apoptotic cells changed from 26.3% in CDDP-treated cells to 40.8% in CCFCA-treated cells. This value was increased to 51.8% in cells treated with CCFCA plus SMF and light irradiation. Precisely, the percentage of apoptotic cells in CCFCA-treated cells under external stimuli (Fig. 6E) was much higher than the percentage of cells that showed mitochondrial membrane depolarization (Fig. 6B) and those that contained active caspase 3 (Fig. 6C). Therefore, the occurrence of other types of cell death which are mitochondria- and caspase-independent signaling pathways like autophagy or ferroptosis is possible.

The modification of the ROS level provides a reasonable strategy to preferentially eliminate cancer cells while avoiding severe harm to normal cells. The capacity of CCFCA to induce ROS stress in cancer cells was examined using the DCFH-DA probe, which can be transformed to fluorescent DCF by ROS. Nanocarrier and CCFCA could meaningfully increase the ROS stress due to the Fenton reaction with endogenous H_2O_2 in cancer cells (Fig. 7A). However, due to the presence of calcium peroxide in the nanocarrier, sufficient H_2O_2 was produced aiming to the performance of Fenton reaction efficiently. On the other hand, besides the tumor-targeting ability of AA in the nanocomposite, it also stimulates cascade reactions, leading to ROS production after entering the cell in the presence of iron. AA plays a role in the production of H_2O_2 by affecting the oxidation level of iron (Hou et al. 2016). Our results also revealed that free CDDP induced moderate ROS stress, mainly through H_2O_2 generation, as previously reported (Kwon et al. 2016). Note that the generation of H_2O_2 and downstream ROS species by CDDP results in severe side effects such as nephrotoxicity and ototoxicity (Ma et al. 2017). Delivery

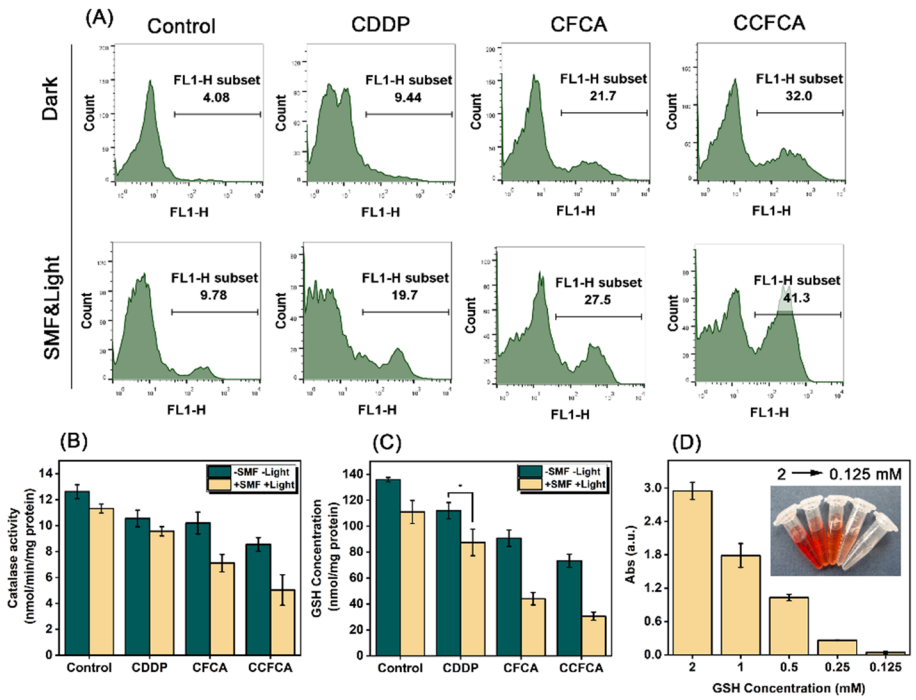

Fig. 7 Disturbance of intracellular redox state in CCFCA-treated cells. **A** Monitoring intracellular ROS in cells treated for 48 h. Evaluation of **B** catalase activity and **C** intracellular GSH levels in CT26 cells treated with CDDP and nanocomposites for 48 h. (D) GSH depletion under the reduction of CCFCA

of CDDP by nanocarrier significantly enhanced DCF fluorescence, indicating the synergized effects between CDDP and iron-based Fenton reaction mediated by nanocarrier in ROS generation. Interestingly, remarkable perturbation in the intracellular redox state was observed as CCFCA-treated cells were exposed to SMF and LED light irradiation. As demonstrated earlier, g-C_3N_4 can be effectively excited under visible light irradiation, producing hydroxyl radicals that disturbed intracellular redox (Fig. 3C and D). Moreover, it has been shown that the loading of cationic metals like Fe_3O_4 on g-C_3N_4 strengthens the photocatalytic performance of g-C_3N_4 due to their narrow energy band gap, enhancing the light absorption range of g-C_3N_4 towards higher wavelength lights (Mirzaei et al. 2019).

Catalase is an essential antioxidant enzyme that decomposes H_2O_2 and protects the cell from its damaging effects. However, limiting the accumulation of H_2O_2 within the tumor cells by catalase activity impedes the generation of toxic hydroxyl radicals catalyzed by the Fenton catalyst, reducing the efficiency of CDT and chemotherapeutic drugs (Lee et al. 2017). The results showed a statistically significant reduction in catalase activity in CDDP and CFCA-treated cells (Fig. 7B). Down-regulation of catalase at the level of protein has been established in CDDP-treated tumor cells (Han et al. 2021). Moreover, Alarifi et al. showed that magnetic nanoparticles cause oxidative stress, DNA damage, and caspase activation in tumor cells by reducing the activities of catalase, superoxide dismutase, and glutathione (Alarifi et al. 2013). A remarkable reduction in catalase activity was observed when cells were treated with CCFCA in the presence and absence of SMF and light irradiation (Fig. 7B). In fact, the defense mechanism was exhausted and the enzyme systems were destroyed owing to the elevated levels of the reactive oxygen species.

One of the most challenging barriers to CDT is high glutathione (GSH) levels in tumor cells with ROS scavenging capabilities (Cao et al. 2022; Cheng et al. 2021). Assessment of intracellular GSH revealed that GSH was significantly consumed in CDDP-treated cells (Fig. 7C). The high concentration of GSH in cancer cells, in addition to protecting cells from high oxidative stress, hinders the efficacy of chemotherapy drugs, including platinum-based medications (Lan et al. 2018). In fact, the thiol group of GSH directly binds to platinum-based drugs and prevents their binding to DNA. Furthermore, a sharp drop in GSH level was observed in cells treated with bare nanocarrier (Fig. 7D). It is due to the reduction of Fe^{3+} on the surface of CFCA by GSH. Greater GSH consumption in response to CCFCA as compared to free CDDP and bare nanocarrier validated the superior nature of drug-loaded nanocomposite to increase the efficacy of CDT. The therapeutic efficiency of photosensitizers in photodynamic therapy also decreases in tumor cells owing to the high content of GSH in tumor cells (Yu et al. 2022). The incorporation of Fe_3O_4 on g-C_3N_4 nanosheets resulted in increased triggered ROS production as well as intracellular GSH depletion (Ju et al. 2016).

3D-in vitro *cytotoxicity studies*

The 3D tumor model also referred to as the multicellular tumor spheroid (MCTS) is proven to have many advantages over the 2D culture for cancer research such as improvement of the structure and cell-to-cell contact that better resemble in vivo architecture and tumor microenvironment (Kang et al. 2020). Therefore, we

developed spheroids as an ex vivo tumor model by a liquid overlay cultivation technique using CT26 cells. The kinetic of spheroid growth and proliferation rate of CT26 cells were analyzed under the influence of free CDDP and CCFCA in the presence and absence of SMF and light irradiation. Based on optical images of spheroids, free CDDP did not exhibit any significant effect on the tumor volume even after 9 days of incubation (Fig. 8A and Additional file 1: Fig. SI12). It has previously been shown that limited drug access to the tumor mass is one of the resistance mechanisms in cancer therapy (Gencoglu et al. 2018). In addition to the drug's inability to pass through the plasma membrane due to its polar nature, suboptimal drug concentrations reached cells within the spheroid core, leading to a reduction of drug cytotoxic efficacy against tumor cells. Exposure of CDDP-treated cells to SMF and light irradiation displayed tumor growth preventing effects after 5 days of incubation as compared to untreated spheroid cells (Fig. 8A). Platinium is a paramagnetic element that might be affected by magnetic fields. In the presence of a magnetic field, the CDDP molecules may move in an ordered manner, causing a change in drug concentration both inside and between cells, resulting in an increase in intracellular CDDP levels (Chen et al. 2010).

Since CDDP was delivered by CFCA nanocarrier, an inhibitory effect on tumor volume was observed after prolonged incubation time (> 5 days); however, much higher tumor regression was achieved in spheroids as they were exposed to CCFCA plus external stimuli (SMF & light) (Fig. 8A and Additional file 1: Fig. SI11). Exposure of CCFCA-treated spheroids to SMF and light irradiation remarkably reduced spheroid volume as compared to that of untreated spheroids. Consistent with these results, the trypan blue exclusion test also revealed that the highest growth rate retardation occurred as spheroid cells were treated with both CCFCA and external stimuli

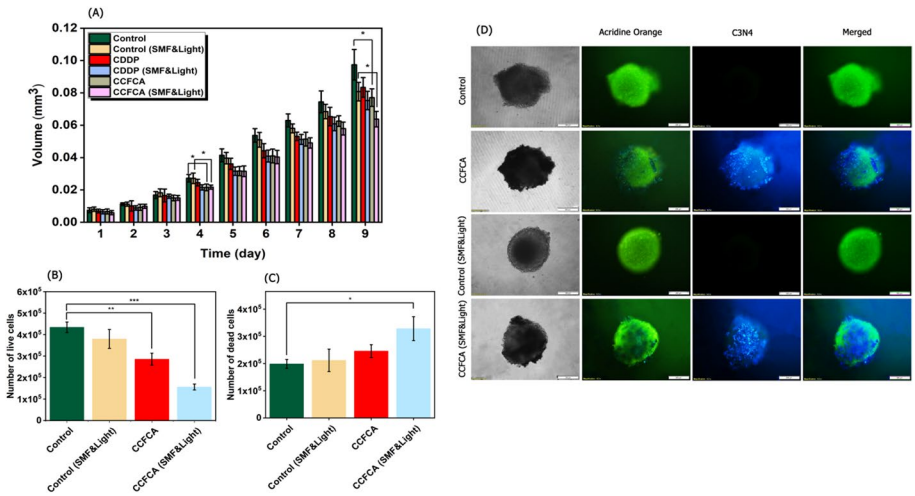

Fig. 8 CT26 spheroid growth profile under the influence of CDDP and CCFCA. **A** The volume of spheroids treated with free CDDP and CCFCA in the presence and absence of SMF and light irradiation. The diameter of at least 30 CT26 spheroids was determined from days 1–9. Evaluation of live **B** and **C** dead cells in treated spheroids after 9 days incubation. **D** Assessment of nanocomposite penetration into spheroids after 3 days of incubation. The emission of green fluorescence is related to acridine orange which stained viable cells and blue fluorescence is related to innate fluorescence emission of nanocomposite (Magnification 100×, Scale bar 200 µm)

(Fig. 8B). At this condition, the reduction of viable cell numbers was accompanied by an increase in dead cell numbers (Fig. 8C).

Certain extracellular matrix components have previously been shown to be highly expressed in the 3D spatial arrangement of spheroids, establishing the penetration barriers found in vivo. Therefore, it is an advantageous approach for investigating the penetration and distribution of CCFCA nanocomposites inside the 3D model (Fig. 8D). In this line, after incubation of spheroids for 3 days with CCFCA, acridine orange staining showed mainly viable proliferating cells (green fluorescence emission) with no dead cells even in the spheroid core, and the nanocomposites were distributed in the outer layers of spheroids (blue fluorescence emission). A different penetration profile was observed as CCFCA-treated spheroids were exposed to SMF and light. Under external stimuli, nanocomposites were mainly concentrated in the core of the spheroids where the number of viable cells decreased. It seems that SMF has a main role in the magnetic nanocomposite trafficking into the spheroid core.

In vivo studies

Considering the deep penetration of nanocomposite into tumor cells and its toxic effects in 2D and 3D in vitro models, in vivo experiments were then carried out to further clarify the targeting and anticancer efficacy of fabricated nanocomposites, using the BALB/c mouse model bearing CT26 cells (Fig. 9A, Additional file 1: Table SI3). As displayed in tumor growth curves (Fig. 9B, C, and Additional file 1: Fig. SI13), tumor

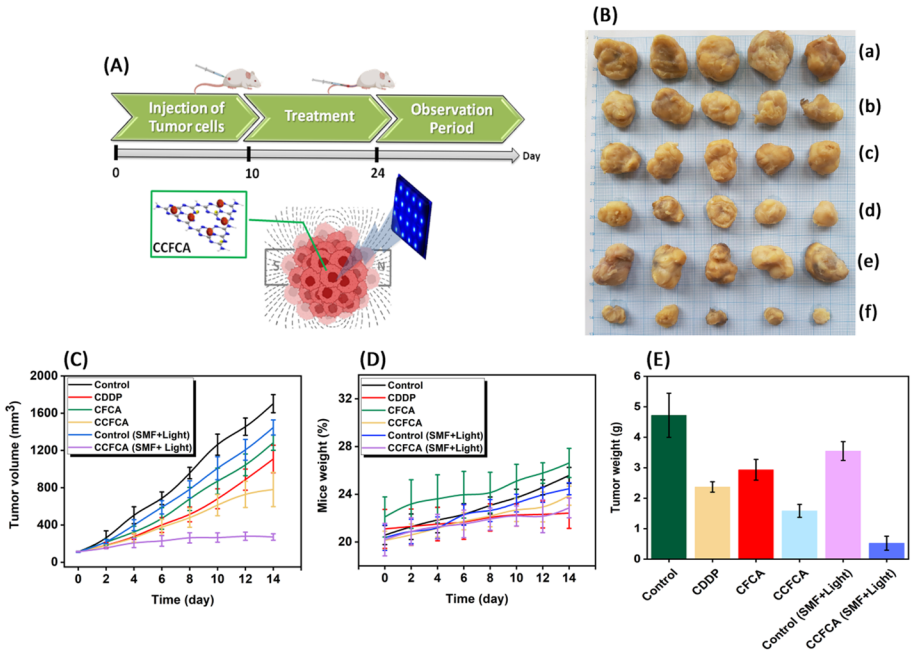

Fig. 9 In vivo antitumor efficacy of free CDDP and CCFCA nanocomposites in CT26 bearing BALB/c mice in the presence and absence of SMF and light irradiation. **A** The schematic representation for the process of tumor induction and drug treatment. **B** The representative excised tumor images, **a** untreated tumor, **b** CDDP, **c** CFCA, **d** CCFCA, **e** SMF & light irradiation, and **f** CCFCA plus SMF & light irradiation treated tumor. **C** Tumor volume, **D** body weight, **E** average tumor weight of treated mice. Note that tumor volume, body weight and average tumor weight were examined during observation period. Data represent mean ± SD ($n = 5$)

volume was decreased to some extent in CDDP-treated mice (1108 ± 147 mm^3) as compared to rapid tumor progression in PBS-treated ones (control) (1702 ± 97 mm^3). However, a significant reduction was observed in tumor volumes of CCFCA-treated mice (780 ± 180 mm^3, $p < 0.0001$ as compared to PBS-treated ones, $p < 0.01$ as compared to CDDP-treated mice), indicating a superior antitumor efficacy contributed from the targeted chemotherapy. Moreover, the mice treated with CDDP showed physical weakness and did not gain weight despite the growth and enlargement of the tumor. At this condition, the weight of the spleen was also remarkably decreased (Additional file 1: Fig. SI13C). These phenomena are inevitable and associated with the side effects of CDDP, while negligible body and spleen weight loss was observed in CCFCA-treated mice. The obtained results showed that targeted delivery of low concentrations of CDDP with a nanosystem reduces the side effects of the drug and improves its effectiveness.

Exposure of PBS-treated mice to SMF and light irradiation led to a statistically significant reduction in tumor volume (1447 ± 80 mm^3) as compared to mice without exposure (1702 ± 97 mm^3). Tumor-reducing effects of the magnetic field have been reported in most in vivo studies; however, it depends on the variety of field strengths, exposure duration, animal models, tumor lines, and other procedure aspects (Gray et al. 2000; Yoshimoto et al. 2022). Moreover, recently it has been well established that LED irradiation at 450 nm decreases tumor size in colon cancer (Yan et al. 2018; Yoshimoto et al. 2022). Therefore, a synergistic effect between SMF and LED irradiation on the reduction of tumor size would be expected. In this line, when mice were treated with CCFCA and exposed to SMF plus light irradiation, a maximum reduction in tumor volume was observed (270 ± 35 mm^3), demonstrating significantly increased therapy effectiveness when compared to various control groups. In fact, the magnetic field improves tumor targeting of magnetic nanosystems and impacts on vibrations of magnetic nanoparticles resulting in localized physical cell damage and eventually killing tumor cells (Li et al. 2017). In addition, g-C_3N_4 in the nanosystem is an active moiety under visible light irradiation, generating ROS in tumor cells and boosting the cytotoxic efficiency of CCFCA.

Based on the histological images shown in Fig. 10A, the number of viable cells significantly decreased in CCFCA-treated tumor cells as compared to that in PBS-treated tumors. Moreover, the nucleus was destroyed, the cell membrane was disrupted, and the characteristics of cell death were observed in CCFCA-treated tumor cells. These phenomena were intensified when the treated tumors were exposed to SMF and LED light radiation. Serious damage was observed in the tissues of mice treated with CDDP. Liver sinusoids became larger and the morphology of the endothelial cells changed. In the spleen tissue, the nuclei of the cells became denser and the cytoplasm decreased. The cube-shaped kidney cells lost their morphology and suffered from severe damage. Accumulation of large nuclei in the lung cells upon treatment with CDDP is due to the inflammation created in this area. Interestingly, no obvious histological changes were observed in the kidney, liver, spleen, and lung tissues of mice treated with CCFCA, particularly in the presence of SMF and light irradiation.

Owing to the innate fluorescence emission of CCFCA, in vivo biodistribution of nanosystem was investigated in treated tumor-bearing mice, using fluorescence in vivo imaging (Fig. 10B and C). It was revealed that the fluorescence signal of the tumor and liver in the experimental group reached the strongest level 24 h post-injection, while an

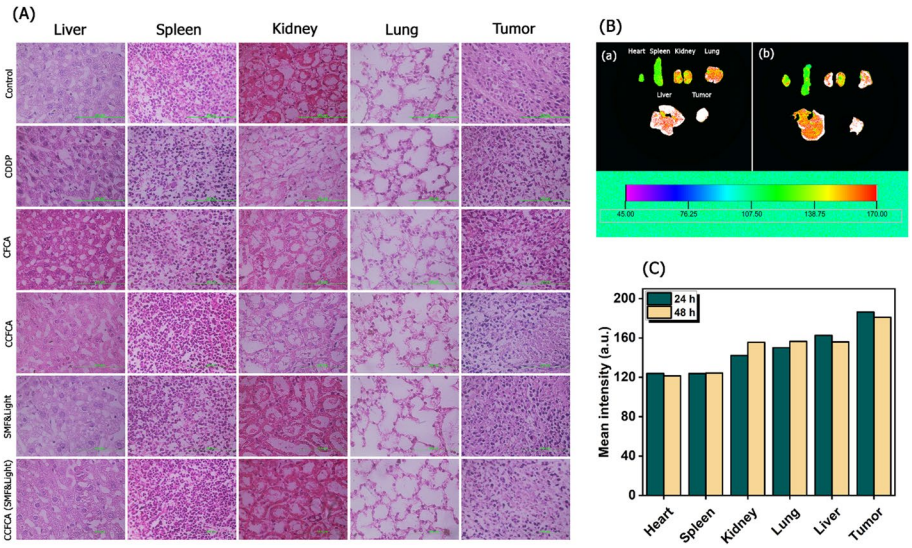

Fig. 10 Representative histological and ex vivo images and mean fluorescence intensity of tumor and main organs. H&E stained histological images were obtained from liver, spleen, kidney, lung, and tumor of CT26 tumor-bearing mice after intravenous administration of free CDDP, bare nanocomposite, and drug-loaded nanocomposites in the presence and absence of SMF & light. **B** Tissues were excited after 24 h (**a**) and 48 h (**b**) of administration of CCFCA and subjected to the imaging equipment. **C** Quantitative analysis of the concentration of CCFCA in tissues after administration of CCFCA

extremely weak fluorescence signal was found in other tissues like the heart, spleen, kidney, and lung. After 48 h, CCFCA was mainly concentrated in the tumor and a moderate signal was detected in lung and kidney tissues. However, no obvious toxicity was observed in in vitro studies on kidney cells (HEK-293 cells) and histological experiments in kidney tissue. It has previously been disclosed that the accumulation of g-C_3N_4 nanosheets in the kidney is due to the elimination route by urinary excretion (Taheri et al. 2020).

Furthermore, the hemocompatibility of nanocomposites was also assessed since nanocomposites encounter the blood cells at a certain stage of their transport through the body (Additional file 1: Table SI4). The routine blood tests indicated that CCFCA has no remarkable effects on the number of red blood cells as compared to the PBS-treated mice, indicating normal hematocrit and no hemolytic effects. In this condition, a slight increase in the number of white blood cells and platelets was observed as compared to healthy mice. This is due to the formation of tumors in these mice, which indicates the early symptoms of cancer in most cases (Mantas et al. 2016; Mehrizi 2021).

Conclusion

Due to the complexity and heterogeneity of TME, surely combined trials are needed for effective cancer therapy. In this study, a multifunctional magnetic nanoplatform (CCFCA) was developed to enhance CDT efficacy against colon cancer with pH-responsive properties, real-time monitoring, and ROS generation characteristics. H_2O_2-self-supplying Fenton nanocatalyst was fabricated and it was accompanied by a chemotherapeutic drug, CDDP. Despite the advantages of CDT for tumor ablation such as high TME selectivity and high capacity for TME modulation, it seems that the

utilization of metal-based Fenton nanocatalysts like CCF nanocomposites that facilitate cancer therapy through the Fenton reaction is not high enough for effective treatment. To achieve superb treatment outcomes in CDT, a photosensitizer, g-C_3N_4, was also added to the nanocomposite translating external energy to highly toxic free radicals within the tumor cells through oxygen-independent type-I PDT. It was a light-mediated Fenton-like reaction which along with an iron-based Fenton reaction made tumor cells vulnerable to chemotherapy. 2D and 3D in vitro experiments and in vivo studies made it evident that CCFCA has biological compatibility, a much higher deep tumor penetration, and cancer cell toxicity than the free drug, particularly in the presence of magnetic field and light irradiation. High elevated levels of ROS generation following the Fenton reaction and PDT overwhelmed the antioxidant defense system (GSH levels and catalase activity) in tumor cells, inducing cell death via apoptosis. In view of all demonstrations above, CCFCA is proven to be a biocompatible nanoplatform that enables the simultaneous application of several other strategies along with CDT to improve the efficacy of cancer treatment.

Abbreviation

AA	Ascorbic acid
AO/EtBr	Acridine orange/ethidium bromide
CDDP	Cisplatin
CCF	CaO_2.CDDP@Fe_3O_4
CCFCA	CaO_2.CDDP@Fe_3O_4.C_3N_4.AA
DI	Deionized water
DMSO	Dimethyl sulfoxide
DCFH-DA	2′,7′ –Dichlorofluorescin diacetate
ELISA	Enzyme-linked immunosorbent assay
FT-IR	Fourier Transform Infrared
GSH	Glutathione
H&E	Hematoxylin and eosin
ICP-OES	Inductively coupled plasma optical emission spectrometer
IC_{50}	The half-maximal inhibitory concentration
MTT	3-(4,5-Dimethylthiazol-2-yl)-2,5-diphenyltetrazolium bromide
MFI	Mean fluorescence intensity
PBS	Phosphate-buffered saline
PI	Propidium iodide
ROS	Reactive oxygen species
SMF	Static magnetic field
S.D.	Standard deviation
VSM	Vibrating sample magnetometer

Supplementary Information

The online version contains supplementary material available at https://doi.org/10.1186/s12645-023-00188-5.

Additional file 1: Figure1 SI1. The percentage of cell viability of NIH3T3 exposed to light at different time intervals. **Table SI1.** The content of CDDP in synthesized nanocomposites measured by ICP-OES analysis. **Figure SI2.** FE-SEM and particle size of fabricated nanocomposites. **Figure SI3.** TEM image of CaO_2.CDDP@Fe_3O_4.C_3N_4.AA (CCFCA). **Figure SI4.** FT-IR spectrum of ascorbic acid. **Figure SI5.** Production of H_2O_2 and hydroxyl radicals under light irradiation. **Figure SI6.** Generation of H_2O_2 and hydroxyl radicals by g-C_3N_4 nanosheets in the presence and absence of light irradiation. **Table SI2.** IC_{50} value of free drug and fabricated samples calculated from treated CT26 cells in the presence and absence of SMF and light irradiation. **Figure SI7.** The viability of CT26 cells under the influence of bare nanocomposite (CFCA) in the presence and absence of SMF and light irradiation. **Figure SI9.** Cell viability of CT26 cells treated with different concentrations of CCFCA nanocomposites after exposure to LED light irradiation for 15 min. **Figure SI10.** CDDP release from CCFCA nanocomposites at different pHs. **Figure SI 11.** (A) photoluminescence spectrum of g-C_3N_4 bulk and sheet. **Figure SI12.** Optical images of MCTS after being treated with free CDDP and CCFCA in the presence and absence of SMF and light irradiation. **Table SI3.** In vivo experiment groups. **Figure SI13.** Tumor inhibition parameters. **Table SI4.** Evaluation of hemocompatibility of CCFCA in healthy and tumor-bearing mice.

Acknowledgements
The authors greatly appreciate the financial support by the Research Council of Ferdowsi University of Mashhad.

Author contributions
LKH: methodology; visualization; validation; formal analysis, and investigation; AM: supervision, project administration, funding acquisition, conceptualization; resources, methodology, visualization, validation, writing original draft-review and editing; MMM: resources, methodology, visualization, validation, writing—review and editing. All authors read and approved the final manuscript.

Funding
This work was supported by Ferdowsi University of Mashhad, grant number: 3.50863.

Availability of data and materials
All data generated or analyzed during this study are included in this published article [and its additional information files].

Declarations

Ethics approval and consent to participate
The animal experiments were carried out following the guidelines approved by animal Ethics Committee of Ferdowsi University of Mashhad (IR.UM.REC. 1399.128).

Consent for publication
All authors consent for the manuscript to be published.

Competing interests
The authors declare no competing financial interest.

Received: 8 March 2023 Accepted: 5 April 2023
Published online: 21 April 2023

References

Alarifi S, Ali D, Suliman AO, Ahamed M, Siddiqui MA, Al-Khedhair AA (2013) Oxidative stress contributes to cobalt oxide nanoparticles-induced cytotoxicity and DNA damage in human hepatocarcinoma cells. Int J Nanomed 8:189–199
Alavi AS, Meshkini A (2018) Fabrication of poly(ethylene glycol)-coated mesoporous nanocomposite ZnO@Fe2O3 for methotrexate delivery: an integrated nanoplatform for dual-mode cancer therapy. Eur J Pharm Sci 115:144–157
An Q, Sun C, Li D, Xu K, Guo J, Wang C (2013) Peroxidase-like activity of Fe3O4@carbon nanoparticles enhances ascorbic acid-induced oxidative stress and selective damage to PC-3 prostate cancer cells. ACS Appl Mater Interfaces 5(24):13248–13257
Cao C, Wang X, Yang N, Song X, Dong X (2022) Recent advances of cancer chemodynamic therapy based on Fenton/Fenton-like chemistry. Chem Sci 13(4):863
Chaudhary S, Smith CA, del Pino P, Fuente JM, Mullin M, Hursthouse A et al (2013) Elucidating the function of penetratin and a static magnetic field in cellular uptake of magnetic nanoparticles. Pharmaceuticals 6(2):204
Chen Q, Espey MG, Sun AY, Pooput C, Kirk KL, Krishna MC et al (2008) Pharmacologic doses of ascorbate act as a prooxidant and decrease growth of aggressive tumor xenografts in mice. Proc Natl Acad Sci USA 105(32):11105–11109
Chen WF, Qi H, Sun RG, Liu Y, Zhang K, Liu JQ (2010) Static magnetic fields enhanced the potency of cisplatin on K562 cells. Cancer Biother Radiopharm 25(4):401–408
Chen D, Xu Q, Wang W, Shao J, Huang W, Dong X (2021) Type I photosensitizers revitalizing photodynamic oncotherapy. Small 17(31):2006742. https://doi.org/10.1002/smll.202006742
Chen F, Yang B, Xu L, Yang J, Li J (2021) A CaO2@tannic acid-feiii nanoconjugate for enhanced chemodynamic tumor therapy. ChemMedChem 16(14):2278–2286. https://doi.org/10.1002/cmdc.202100108
Chen X, Wang L, Liu S, Luo X, Wang K, He Q (2022) Cisplatin-loaded metal–phenolic network with photothermal-triggered ROS generation for chemo-photothermal therapy of cancer. Cancer Nanotechnol. 13(1):1–16. https://doi.org/10.1186/s12645-022-00149-4
Cheng X, Xu HD, Ran HH, Liang G, Wu FG (2021) Glutathione-depleting nanomedicines for synergistic cancer therapy. ACS Nano 15(5):8039–8068
Choi KH, Nam KC, Kim UH, Cho G, Jung JS, Park BJ (2017) Optimized photodynamic therapy with multifunctional cobalt magnetic nanoparticles. Nanomater 7:6
Correia JH, Rodrigues JA, Pimenta S, Dong T, Yang Z. Photodynamic Therapy review: principles, photosensitizers, applications, and future directions. pharmaceutics . Multidisciplinary Digital Publishing Institute (MDPI); 2021;13:9.
Cui X, Zhang J, Wan Y, Fang F, Chen R, Shen D et al (2019) Dual fenton catalytic nanoreactor for integrative type-i and type-ii photodynamic therapy against hypoxic cancer cells. ACS Appl 2(9):3854–3860
Cui L, Liu Y, Fang X, Yin C, Li S, Sun D, et al. Scalable and clean exfoliation of graphitic carbon nitride in NaClO solution: enriched surface active sites for enhanced photocatalytic H2 evolution. Green Chem. . 2018;20(6):1354–61. https://pubs.rsc.org/en/content/articlehtml/2018/gc/c7gc03704j
Dai X, Du T, Han K (2019) Engineering nanoparticles for optimized photodynamic therapy. ACS Biomater Sci Eng 5(12):6342–6354. https://doi.org/10.1021/acsbiomaterials.9b01251

Davardoostmanesh M, Ahmadzadeh H, Goharshadi EK, Meshkini A, Sistanipour E (2020) Graphitic carbon nitride nanosheets prepared by electrophoretic size fractionation as an anticancer agent against human bone carcinoma. Mater Sci Eng C 111:110803

Fattahimoghaddam H, Mahvelati-Shamsabadi T, Lee BK (2021) Enhancement in photocatalytic H2O2 production over g-C3N4 nanostructures: a collaborative approach of nitrogen deficiency and supramolecular precursors. ACS Sustain. Chem. Eng. 9(12):4520–4530. https://doi.org/10.1021/acssuschemeng.0c08884

Gao S, Lu X, Zhu P, Lin H, Yu L, Yao H, et al. Self-evolved hydrogen peroxide boosts photothermal-promoted tumor-specific nanocatalytic therapy. J. Mater. Chem. B . 2019;7(22):3599–609. https://pubs.rsc.org/en/content/articlehtml/2019/tb/c9tb00525k

Gencoglu MF, Barney LE, Hall CL, Brooks EA, Schwartz AD, Corbett DC et al (2018) Comparative study of multicellular tumor spheroid formation methods and implications for drug screening. ACS Biomater Sci Eng 4(2):410–420

Gray JR, Frith CH, Parker JD (2000) In vivo enhancement of chemotherapy with static electric or magnetic fields. Bioelectromagnetics 21(8):575–583

Güney G, Kutlu HM, Genç L (2014) Preparation and characterization of ascorbic acid loaded solid lipid nanoparticles and investigation of their apoptotic effects. Colloids Surfaces B Biointerfaces. 121:270–280

Hajipour Verdom B, Abdolmaleki P, Behmanesh M. The Static Magnetic Field Remotely Boosts the Efficiency of Doxorubicin through Modulating ROS Behaviors. Sci. Reports 2018 81 . 2018;8(1):1–12. https://www.nature.com/articles/s41598-018-19247-8

Han YK, Kim JS, Jang GB, Park KM (2021) Cisplatin induces lung cell cilia disruption and lung damage via oxidative stress. Free Radic Biol Med 177:270–277

He J, Fu LH, Qi C, Lin J, Huang P (2021) Metal peroxides for cancer treatment. Bioact Mater. 6(9):2698–2710

Hou X, Shen W, Huang X, Ai Z, Zhang L (2016) Ascorbic acid enhanced activation of oxygen by ferrous iron: a case of aerobic degradation of rhodamine B. J Hazard Mater 308:67–74

Huang L, Jiang S, Cai B, Wang G, Wang Z, Wang L (2021) pH-Triggered nanoreactors as oxidative stress amplifiers for combating multidrug-resistant biofilms. Chem Commun57(38):4662–5. https://pubs.rsc.org/en/content/articlehtml/2021/cc/d1cc00247c

Izadi A, Meshkini A, Entezari MH (2019) Mesoporous superparamagnetic hydroxyapatite nanocomposite: a multifunctional platform for synergistic targeted chemo-magnetotherapy. Mater Sci Eng C 101:27–41

Ju E, Dong K, Chen Z, Liu Z, Liu C, Huang Y et al (2016) Copper(II)–graphitic carbon nitride triggered synergy: improved ROS generation and reduced glutathione levels for enhanced photodynamic therapy. Angew Chemie 55(38):11467–11471

Kang Y, Datta P, Shanmughapriya S, Ozbolat IT (2020) 3D bioprinting of tumor models for cancer research. ACS Appl Bio Mater 3(9):5552–5573

Khorshidi S, Karkhaneh A, Bonakdar S (2020) Fabrication of amine-decorated nonspherical microparticles with calcium peroxide cargo for controlled release of oxygen. J Biomed Mater Res A 108(1):136–147

Khoshtabiat L, Meshkini A, Matin MM (2021) Fenton-magnetic based therapy by dual-chemodrug-loaded magnetic hydroxyapatite against colon cancer. Mater Sci Eng C Mater Biol Appl 127:1.

Kruger NJ (1994) The Bradford method for protein quantitation. Methods Mol Biol 32:9–15

Kwon B, Han E, Yang W, Cho W, Yoo W, Hwang J et al (2016) Nano-fenton reactors as a new class of oxidative stress amplifying anticancer therapeutic agents. ACS Appl Mater Interfaces 8(9):5887–5897

Lan D, Wang L, He R, Ma J, Bin Y, Chi X et al (2018) Exogenous glutathione contributes to cisplatin resistance in lung cancer A549 cells. Am J Transl Res. 10(5):1295

Lee KT, Lu YJ, Mi FL, Burnouf T, Wei YT, Chiu SC et al (2017) Catalase-modulated heterogeneous fenton reaction for selective cancer cell eradication: SnFe2O4 nanocrystals as an effective reagent for treating lung cancer cells. ACS Appl Mater Interfaces 9(2):1273–1279

Li WP, Su CH, Chang YC, Lin YJ, Yeh CS (2016) Ultrasound-induced reactive oxygen species mediated therapy and imaging using a fenton reaction activable polymersome. ACS Nano 10(2):2017–2027. https://doi.org/10.1021/acsnano.5b06175

Li SL, Jiang P, Jiang FL, Liu Y (2021) Recent advances in nanomaterial-based nanoplatforms for chemodynamic cancer therapy. Adv Funct Mater 31(22):2100243. https://doi.org/10.1002/adfm.202100243

Li W, Liu Y, Qian Z, Yang Y (2017) Evaluation of tumor treatment of magnetic nanoparticles driven by extremely low frequency magnetic field. Sci Rep 7(1):1–9. https://www.nature.com/articles/srep46287

Liu J, Liu Y, Liu N, Han Y, Zhang X, Huang H et al (2015) Metal-free efficient photocatalyst for stable visible water splitting via a two-electron pathway. Science 347(6225):970–974. https://doi.org/10.1126/science.aaa3145

Liu J, Zhu C, Xu L, Wang D, Liu W, Zhang K et al (2020) Nanoenabled intracellular calcium bursting for safe and efficient reversal of drug resistance in tumor cells. Nano Lett. https://doi.org/10.1021/acs.nanolett.0c03042

Liu P, Peng Y, Ding J, Zhou W (2022) Fenton metal nanomedicines for imaging-guided combinatorial chemodynamic therapy against cancer. Asian J Pharm Sci 17(2):177–192

Lopez S, Hallali N, Lalatonne Y, Hillion A, Antunes JC, Serhan N, et al. (2022) Magneto-mechanical destruction of cancer-associated fibroblasts using ultra-small iron oxide nanoparticles and low frequency rotating magnetic fields. Nanoscale Adv 4(2):421–36. https://pubs.rsc.org/en/content/articlehtml/2022/na/d1na00474c

Ma P, Xiao H, Yu C, Liu J, Cheng Z, Song H et al (2017) Enhanced cisplatin chemotherapy by iron oxide nanocarrier-mediated generation of highly toxic reactive oxygen species. Nano Lett 17(2):928–937

Mantas D, Kostakis ID, Machairas N, Markopoulos C (2016) White blood cell and platelet indices as prognostic markers in patients with invasive ductal breast carcinoma. Oncol Lett 12(2):1610–1614

Mehrizi TZ (2021) Hemocompatibility and hemolytic effects of functionalized nanoparticles on red blood cells: a recent review study. NANO 16:8

Meshkini A, Oveisi H (2017) Methotrexate-F127 conjugated mesoporous zinc hydroxyapatite as an efficient drug delivery system for overcoming chemotherapy resistance in osteosarcoma cells. Colloids Surf B Biointerfaces 158:319–330

Mirzaei A, Chen Z, Haghighat F, Yerushalmi L (2019) Magnetic fluorinated mesoporous g-C3N4 for photocatalytic degradation of amoxicillin: transformation mechanism and toxicity assessment. Appl Catal B Environ 242:337–348

Murros K, Wasiljeff J, Macías-Sánchez E, Faivre D, Soinne L, Valtonen J et al (2019) Magnetic nanoparticles in human cervical skin. Front Med 6:123

Ngo B, Van Riper JM, Cantley LC, Yun J (2019) Targeting cancer vulnerabilities with high-dose vitamin C. Nat Rev Cancer 19(5):271–282
Pereira PMR, Berisha N, Bhupathiraju NV, Fernandes R, Tomé JPC, Drain CM (2017) Cancer cell spheroids are a better screen for the photodynamic efficiency of glycosylated photosensitizers. PLoS ONE 12:5
Ranji-Burachaloo H, Reyhani A, Gurr PA, Dunstan DE, Qiao GG. Combined Fenton and starvation therapies using hemoglobin and glucose oxidase. Nanoscale . 2019;11(12):5705–16. https://pubs.rsc.org/en/content/articlehtml/2019/nr/c8nr09107b
Rao S, Li Y, Liu H, Gao S, Zhao J, Rahman N et al (2021) Polyethyleneimine induced highly dispersed Ag nanoparticles over g-C3N4 nanosheets for efficient photocatalytic and antibacterial performance. Ceram Int 47(6):8528–8537
Seabra AB (2017) Iron oxide magnetic nanoparticles in photodynamic therapy: A promising approach against tumor cells. Met Nanoparticles Pharma. 1:3–20. https://doi.org/10.1007/978-3-319-63790-7_1
Song X, Chen P, Luo X, Zhang Y, Liu J (2019) ··A novel laminated Fe3O4/CaO2 composite for ultratrace arsenite oxidation and adsorption in aqueous solutions. J Environ Chem Eng 7(5):103427
Sreeja V, Jayaprabha KN, Joy PA (2015) Water-dispersible ascorbic-acid-coated magnetite nanoparticles for contrast enhancement in MRI. Appl Nanosci 5(4):435–441. https://doi.org/10.1007/s13204-014-0335-0
Tabish TA, Hamblin MR (2021) Mitochondria-targeted nanoparticles (mitoNANO): an emerging therapeutic shortcut for cancer. Biomater Biosyst. 3:100023
Taheri H, Unal MA, Sevim M, Gurcan C, Ekim O, Ceylan A et al (2020) Photocatalytically active graphitic carbon nitride as an effective and safe 2d material for in vitro and in vivo photodynamic therapy. Small 16(10):1904619. https://doi.org/10.1002/smll.201904619
Tang Z, Zhao P, Wang H, Liu Y, Bu W (2021) Biomedicine meets fenton chemistry. Chem Rev 121(4):1981–2019. https://doi.org/10.1021/acs.chemrev.0c00977
Tian Q, Xue F, Wang Y, Cheng Y, An L, Yang S, et al. (2021) Recent advances in enhanced chemodynamic therapy strategies. Nano Today 39:101162. https://www.sciencedirect.com/science/article/pii/S1748013221000876
Wang JC, Cui CX, Kong QQ, Ren CY, Li Z, Qu L et al (2018) Mn-doped g-C3N4 nanoribbon for efficient visible-light photocatalytic water splitting coupling with methylene blue degradation. ACS Sustain Chem Eng. 6(7):8754–8761. https://doi.org/10.1021/acssuschemeng.8b01093
Xu J, Shamul JG, Kwizera EA, He X (2022) Recent advancements in mitochondria-targeted nanoparticle drug delivery for cancer therapy. Nanomaterials 12(5):743
Yadav P, Mimansa A, Kailasam K, Shanavas A (2022) Nontoxic metal-free visible light-responsive carbon nitride quantum dots cause oxidative stress and cancer-specific membrane damage. ACS Appl Bio Mater 5(3):1169–1178. https://doi.org/10.1021/acsabm.1c01219
Yan G, Zhang L, Feng C, Gong R, Idiiatullina E, Huang Q et al (2018) Blue light emitting diodes irradiation causes cell death in colorectal cancer by inducing ROS production and DNA damage. Int J Biochem Cell Biol 103:81–88
Yao C, Rudnitzki F, Hüttmann G, Zhang Z, Rahmanzadeh R (2017) Important factors for cell-membrane permeabilization by gold nanoparticles activated by nanosecond-laser irradiation. Int J Nanomed 12:5659–5672
Yoshimoto T, Shimada M, Tokunaga T, Nakao T, Nishi M, Takasu C et al (2022) Blue light irradiation inhibits the growth of colon cancer and activation of cancer-associated fibroblasts. Oncol Rep 47:5
Youssef Z, Vanderesse R, Colombeau L, Baros F, Roques-Carmes T, Frochot C et al (2017) The application of titanium dioxide, zinc oxide, fullerene, and graphene nanoparticles in photodynamic therapy. Cancer Nanotechnol. 8(1):1–62. https://doi.org/10.1186/s12645-017-0032-2
Yu J, Xiao H, Yang Z, Qiao C, Zhou B, Jia Q et al (2022) A potent strategy of combinational blow toward enhanced cancer chemo-photodynamic therapy via sustainable GSH elimination. Small 18:9
Zhang Y, Cheng Y, Yang F, Yuan Z, Wei W, Lu H et al (2020) Near-infrared triggered Ti3C2/g-C3N4 heterostructure for mitochondria-targeting multimode photodynamic therapy combined photothermal therapy. Nano Today 34:1
Zhao X, Liu J, Fan J, Chao H, Peng X. Recent progress in photosensitizers for overcoming the challenges of photodynamic therapy: from molecular design to application. Chem Soc Rev. 2021;50(6):4185–219. https://pubs.rsc.org/en/content/articlehtml/2021/cs/d0cs00173b
Zingale E, Romeo A, Rizzo S, Cimino C, Bonaccorso A, Carbone C et al (2022) Fluorescent nanosystems for drug tracking and theranostics: recent applications in the ocular field. Pharmaceutics 14:5

Publisher's Note